Computational Studies of Electrode Materials in Sodium-Ion Batteries

Qiang Bai, Lufeng Yang, Hailong Chen, and Yifei Mo**

Sodium-ion batteries have attracted extensive interest as a promising solution for large-scale electrochemical energy storage, owing to their low cost, materials abundance, good reversibility, and decent energy density. For sodium-ion batteries to achieve comparable performance to current lithium-ion batteries, significant improvements are still required in cathode, anode, and electrolyte materials. Understanding the functioning and degradation mechanisms of the materials is essential. Computational techniques have been widely applied in tandem with experimental investigations to provide crucial fundamental insights into electrode materials and to facilitate the development of materials for sodium-ion batteries. Herein, the authors review computational studies on electrode materials in sodium-ion batteries. The authors summarize the current state-of-the-art computational techniques and their applications in investigating the structure, ordering, diffusion, and phase transformation in cathode and anode materials for sodium-ion batteries. The unique capability and the obtained knowledge of computational studies as well as the perspectives for sodium-ion battery materials are discussed in this review.

1. Introduction

The fast-growing energy generation from renewable sources such as solar, wind, and wave is calling for reliable energy storage technologies with high energy density, high power, and low cost, because the electricity harvested from these renewable energy sources are intermittent.[1] While Li-ion batteries (LIBs) may serve this purpose owing to their high energy density and long cycle life, current LIBs are still too expensive for large-scale grid-level storage.[2] Na-ion battery (NIB) is a promising, cheaper alternative to LIB for rechargeable energy storage. NIB owns the following advantages in cost over LIB.[2] Na is highly abundant in the Earth's crust, compared to relatively scarce lithium, which is concentrated in limited geological regions.[2] Inexpensive and lightweight aluminum can be used as current collectors in NIBs to replace the heavier and more expensive copper used at the anode side in LIBs.[3] Furthermore, the expensive transition metal elements that are heavily used in the cathodes of LIBs, such as Co and Ni, may be replaced by much less expensive elements, such as Mn and Fe, in NIBs.[2,4]

NIB shares similar functioning mechanism as LIB, as Na ions shuttling between two Na-ion hosting electrodes through an organic liquid electrolyte under cycling voltage.[5] Currently, the performance of NIBs, including energy density, power density, and cycle life, at laboratory scale, is nearly comparable to that of commercial LIBs.[6–8] For example, a number of layered oxide cathodes are demonstrated with a high capacity of 190 mA h g^{-1},[7,9] a high rate of 30 C,[10] and a long cycle life of a few hundred cycles.[11] Recent research efforts in NIBs demonstrated the promise of building NIB systems that have performance comparable to LIBs.

The similarity in the operational mechanisms of NIBs and LIBs serves as a good foundation for the research and development of NIBs. However, the differences between Na and Li lead to many challenges and new opportunities for NIBs. The sodiation potentials are often lower than the lithiation potentials in the same materials, leading to lower voltages in NIBs than in LIBs.[12] In addition, there is a common myth that the Na ion, with its larger radius, is expected to exhibit slower diffusion kinetics than the Li ion. However, the much larger chemical space of sodium compounds compared to the lithium counterparts offers many opportunities to overcome these aforementioned challenges. For example, while only a few transition metals form electrochemically active lithium layered oxides,[12–14] such as $LiCoO_2$ and $LiNiO_2$, more transition metals, such as Fe,[15] Co,[16] Mn,[17] Ni,[18] Cr,[13,18] Ti,[19] etc., can form sodium layered oxides, which have a number of layered structure polymorphs with demonstrated good battery performance.[20]

Q. Bai, Prof. Y. Mo
Department of Materials Science and Engineering
University of Maryland
College Park, MD 20742, USA
E-mail: yfmo@umd.edu

Prof. Y. Mo
Maryland Energy Innovation Institute
University of Maryland
College Park, MD 20742, USA

Dr. L. Yang, Prof. H. Chen
The Woodruff School of Mechanical Engineering
Georgia Institute of Technology
Atlanta, GA 30332, USA
E-mail: hailong.chen@me.gatech.edu

The ORCID identification number(s) for the author(s) of this article can be found under https://doi.org/10.1002/aenm.201702998.

DOI: 10.1002/aenm.201702998

Computational modeling has been widely employed for the understanding, design, and discovery of electrode materials in NIBs. First principles computations based on density functional theory (DFT) have been demonstrated in evaluating a wide range of essential battery-related properties, such as voltage,[12] theoretical capacity,[21] theoretical energy density,[22] ion diffusion,[23] phase stability,[12,24] etc. Multiple new electrode and solid electrolyte materials for NIBs have been predicted by first principles computation techniques.[23,25–31] These highly scalable computational approaches are also advantageous in quickly screening, discovering, and predicting new sodium-containing compounds with desirable merits for NIBs.[32,33] Furthermore, computational studies provide unique understanding into the fundamental mechanisms specific to sodium electrode materials during electrochemical cycling. For example, since Na layered oxides exhibit more stable polymorphs and more Na orderings at various sodiation levels, the phase evolution of these materials in the electrochemical sodiation and desodiation processes is more complex than that in LIBs.[34,35] To study and understand these complex structures and mechanisms, computational modeling can provide valuable insights and knowledge about the structures, thermodynamics, diffusion kinetics, and phase transformations, greatly complementing experimental characterization and accelerating the research processes. Given the ever-rising importance and contribution of computational studies to the research of NIBs, we review the recent development and progress in computational studies of the electrode materials in NIBs. This review highlights the contribution and the potential of computational studies in further facilitating and accelerating the research and development of materials for NIBs.

2. Computational Methods

In this section, we summarize computational methods that are used for studying electrode materials in NIBs. Many of these computation techniques are standard in studying battery materials,[23,36–38] and further technical details for these computational methods can be found in other reviews[39–42] and studies cited in specific sections.

2.1. Structure and Energy

2.1.1. Equilibrium Voltage and Voltage Profile

The overall cell reaction, combining anode and cathode reactions of a cathode material Na_xA and Na metal anode during the sodiation, can be considered as

$$Na_{x_1}A + (x_2 - x_1)Na \rightarrow Na_{x_2}A \quad (1)$$

where the cathode material is sodiated from $Na_{x_1}A$ to $Na_{x_2}A$ by inserting $x_2 - x_1$ Na from the Na metal anode. The averaged equilibrium voltage V referenced to Na/Na$^+$ is calculated as the reaction Gibbs free energy ΔG_r over the number of Na ions transferred

Qiang Bai received his B.S. degree in Materials Science and Engineering from Nanjing University, China in 2015. He is currently a graduate student at the Department of Materials Science and Engineering in the University of Maryland, College Park, USA, under the supervision of Prof. Yifei Mo. His current research focuses on the computational design for energy storage and conversion materials.

Hailong Chen is an Assistant Professor of the Woodruff School of Mechanical Engineering at Georgia Institute of Technology. He received his B.S. and M.S. from Tsinghua University and Ph.D. from Stony Brook University. His research interests include design of novel electrode materials for Li-ion and Na-ion batteries and solid-state electrolytes with using combined computational and experimental approaches. His research also focuses on development of in situ X-ray structural characterization techniques.

Yifei Mo is an Assistant Professor of Materials Science and Engineering at the University of Maryland, College Park, USA. He received his B.S. from Peking University and Ph.D. from the University of Wisconsin-Madison, and conducted his postdoctoral research at Massachusetts Institute of Technology. His research aims to advance the understanding, design, and discovery of engineering materials through computational techniques, with current emphases on critical materials problems in beyond Li-ion and all-solid-state batteries.

$$V = -\frac{\Delta G_r}{(x_2 - x_1)F} = -\frac{G(Na_{x_2}A) - G(Na_{x_1}A) - (x_2 - x_1)G(Na)}{(x_2 - x_1)F} \quad (2)$$

where G refers to the Gibbs free energy of the corresponding phase and F is the Faraday constant. In most current first principles computation studies,[12,42] ΔG_r is approximated by the reaction internal energy (Equation (3)) calculated at 0 K, as the contributions from entropy and volume changes are small at low temperatures and often cancelled out. Using the internal energies from static first principles computation, the equilibrium voltage is calculated as

$$V = -\frac{E\left(\mathrm{Na}_{x_2}\mathrm{A}\right)-E\left(\mathrm{Na}_{x_1}\mathrm{A}\right)-\left(x_2-x_1\right)E(\mathrm{Na})}{\left(x_2-x_1\right)F} \tag{3}$$

where internal energies E of $\mathrm{Na}_{x_2}\mathrm{A}$, $\mathrm{Na}_{x_1}\mathrm{A}$, and bulk Na are from first principles calculations at 0 K.

The electrode materials, for example, layered Na transition-metal oxides Na_xMO_2[37,43] and Na-based alloys,[22] may exhibit stable phases at their intermediate Na concentrations. As a result, there may be multiple voltage plateaus during the electrochemical cycling. The equilibrium voltage between each pair of adjacent intermediate stable phases can be calculated using Equation (3), and the voltage profiles as a function of Na concentrations can be constructed from these voltages. Therefore, in order to construct the voltage profile, one needs to identify the intermediate stable phases of an electrode as a function of Na concentrations.

2.1.2. Stable Phases and Na-Ion Ordering

First principles computation has been widely used in identifying and predicting these intermediate stable phases as a function of Na concentration in parallel with direct experimental characterizations.[22,37,38] For example, multiple intermediate phases, such as $NaPb_3$, NaPb, Na_5Pb_2, and $Na_{15}Pb_4$, can form in Na–Pb alloying electrode.[22,44] The layered oxides Na_xMO_2 with M = Ti, V, Cr, Mn, Fe, Co, Ni, as cathode materials for NIBs are known to exhibit a number of stable intermediate states with different Na-vacancy orderings at different Na concentrations x.[37,45] In these intercalation compounds, only a fraction of Na sites are occupied, leading to a large number of possible configurations of Na ions and vacancies.

To identify these different Na orderings, computation studies are often performed first to enumerate many different Na-vacancy configurations and then to identify the structures with the lowest energy. Given a large number of possible configurations, a common practice is to first rank the enumerated configurations by electrostatic energy obtained from preassumed atomic charges,[42,46] as physically stable structures are unlikely to have high electrostatic energy, and then to perform DFT calculations on a fraction (often ≈10–100) of those configurations with the lowest electrostatic energies. The structures with the lowest DFT energies for each composition are then identified.

To compare the relative stability of these configurations, the formation energy of the given Na_xMO_2 composition can be calculated as

$$E_{\mathrm{f}} = E\left(\mathrm{Na}_x\mathrm{MO}_2\right)-xE\left(\mathrm{NaMO}_2\right)-(1-x)E\left(\mathrm{MO}_2\right) \tag{4}$$

referencing to the sodiated $NaMO_2$ and desodiated MO_2 phases. The convex hull of the formation energies of all these structures is constructed as a function of Na concentrations x. The thermodynamically stable phases are identified from the energy convex hull. All stable phases identified are based on static first principles calculations corresponding to 0 K ground states, and so are the calculated voltage profiles.

2.1.3. Stable Phases and Voltage Profile at Finite Temperatures

Monte Carlo (MC) modeling is capable of evaluating structures and energies at finite temperatures by including the configurational entropy contribution.[36] In MC modeling, a large number of energy evaluations often based on the cluster expansion approach are sampled for different configurations.[36,43,47,48] The cluster expansion method provides a lattice-based Hamiltonian fitted to DFT energies and is significantly more efficient in computation costs. Based on the cluster-expansion Hamiltonian, MC modeling can study Na orderings at finite temperatures and obtain finite-temperature phase diagrams. The technical details of cluster-expansion-based MC modeling can be found in another review[42] and the literature.[36,43,47,48]

2.1.4. Errors of DFT Calculations

The evaluation of Na-vacancy ordering, stable phase, structure, cell voltage, and voltage profile requires accurate energies from first principles calculations. The quantitative inaccuracy of first principles calculations is a general problem caused by self-interaction errors in DFT,[49,50] where the unphysical interactions of each electron are not fully cancelled. In the commonly used semi-local functionals based on local density approximation (LDA) and generalized gradient approximation (GGA), the self-interaction errors result in an artificial delocalization of electrons causing significant errors in the systems with strongly correlated electrons, such as transition metals.[49,50] DFT+U method[51–53] using a Hubbard U term is a widely adopted practical approach to correct the self-interaction errors, as it does not require notably more computational time. A Hubbard U parameter for each element with strong correlated electrons can be determined from linear response theory[50,54] or from fitting to reference properties, such as band structures and formation energies.[55,56] DFT+U methods have been benchmarked and widely used in the study of LIB materials.[55,57,58] In the studies of cathode materials in LIBs, the voltages calculated based on DFT+U approximation are in better agreement with experimental values than those based on GGA or LDA functionals without Hubbard U.[55,57] For many electrode materials with transition metals in NIBs, the use of DFT+U has a significant impact on the computation results.[36,43] A comparison of the results from different approaches is provided in Section 3.1.2.

Another source of error from DFT calculations is the absence of van de Waals (vdW) interactions.[59,60] The commonly used LDA and GGA functionals neglect the long-range vdW interactions.[59,60] For the materials systems commonly studied for NIBs, the long-range vdW interactions are important to properly describe the structures and energies of layered materials[61–65] and organic molecular materials.[66,67] A number of vdW corrections, including semiempirical corrections (e.g., DFT-D,[68] DFT-D2,[69] DFT-D3[70]) and vdW functionals (e.g., vdW-DF,[71] vdW-DF2,[72] and vdW-optPBE[73]), have been developed for the DFT computation scheme. For example, the

DFT-D method includes long-range dispersion interactions with the coefficient for each pair of atomic species, and these coefficients in DFT-D are predetermined constants.[68] The vdW-DF method instead determines the dispersion interactions directly from the electron density[71]: nonlocal, long-range correlations from vdW interactions were added into the semi-local correlation functionals. The vdW corrections show significant improvements in reproducing the lattice parameters and the formation energies of layered materials (e.g., graphite[63] and polysilane[65]) and organic molecular materials (e.g., $Na_xC_6O_6$[66] and $Na_xC_6Cl_4O_2$[67]). In addition, the energies of adsorption and intercalation, e.g., in graphite[61,62] and phosphorene,[64] are also improved by the use of vdW corrections. Therefore, the use of vdW corrections should be considered and tested for layered and organic molecular materials.

2.2. Diffusion

2.2.1. Ion Migration Pathway and Energy Barrier

The nudged elastic band (NEB) method[39,74] is a widely used approach for studying the atomistic diffusion mechanism. NEB calculation is performed on a particular ion-migration pathway from the initial to the final equilibrium site. NEB calculations require initial guesses of these atomistic migration mechanisms as input. Based on the initial guesses of the migration mechanism, NEB calculations can identify the lowest energy migration pathway, the energy profile along the pathway, the transition state, and the migration energy barrier. The climbing-image NEB method[75] incorporates a modification of NEB method to obtain the highest image at the saddle point and thus obtain a more accurate estimation of transition state and migration energy barrier. In this review, we use the term of NEB to represent both methods, as recent NEB calculations were performed using the climbing-image NEB method.[38,76]

The construction of NEB calculations may be difficult for studying the complex diffusion mechanism in many NIB electrode materials that have structures with many symmetrically distinctive Na sites and diverse Na orderings. For example, many layered Na_xMO_2 oxides have complex Na orderings at different Na concentrations, leading to complex diffusion mechanisms.[23] While one can perform NEB calculations for all possible Na^+ diffusion pathways, it is difficult to guess a priori whether a diffusion mode would actually happen and which diffusion mode is dominant. For studying materials with complex diffusion mechanisms, NEB calculations are greatly complemented by molecular dynamics (MD) simulations.

2.2.2. Molecular Dynamics Simulations

MD simulations[39,42] model the real-time Newtonian dynamics of all atoms in the materials, and thus fully capture the diffusion of ions. By tracking the real-time trajectories and displacements of Na ions in MD simulations, the rate of diffusion over time can be quantified by the mean square displacement

$$\left\langle [\Delta r(t)]^2 \right\rangle = \frac{1}{N}\sum_i \left\langle [r_i(t+t_0) - r_i(t_0)]^2 \right\rangle \tag{5}$$

where N is the total number of Na ions and $r_i(t)$ corresponds to the displacement of the i-th Na ion at the time t. The arrow bracket represents the average over different starting time t_0. The self-diffusivity D^* of Na^+ can be obtained as[39,77]

$$D^* = \frac{1}{2dt}\left\langle [\Delta r(t)]^2 \right\rangle \tag{6}$$

where d is the dimension of the lattice for diffusion. The ionic conductivity σ is estimated based on the Nernst–Einstein equation[39,42]

$$\sigma = \frac{Ne^2}{V\,k_B T} D \tag{7}$$

where N is the total number of mobile Na ions, V is the volume of the simulation cell, e is the Na-ion charge, and T is the temperature. In a material where the hopping of different Na ions is independent from each other, the self-diffusion diffusivity D^* obtained from MD simulations can be used to evaluate the ionic conductivity. Otherwise, the correlation factor of Na ion diffusion should be considered.[42,78]

In addition, MD simulations are performed at multiple temperatures to obtain the diffusivities and ionic conductivities at multiple temperatures, similar to experimental measurements. If the same diffusion mechanism holds over the temperature range, the diffusivity follows the Arrhenius relation

$$D(T) = D_0 e^{-\frac{E_a}{k_B T}} \tag{8}$$

where E_a is the activation energy. In MD simulations, the activation energy for overall ion transport is obtained by fitting the Arrhenius relation (Equation (8)). In addition, the diffusivity and corresponding conductivity at other temperatures can be estimated by extrapolating the Arrhenius relation.

NEB calculations and MD simulations can be performed using either DFT methods[12,23] or classical potentials (also known as force fields).[40,79] NEB calculations are mostly performed using DFT methods, which provide more reliable potential energy surface and more accurate migration energy barrier.[12,23,38] While MD simulations were traditionally performed using classical potentials,[40] ab initio MD (AIMD) simulations based on DFT to calculate the interatomic interactions have recently gained great successes in quantifying diffusional properties and in identifying diffusion mechanisms.[23,80,81] However, given the significantly higher computational cost of AIMD simulations compared to classical MD simulations, AIMD simulations are often limited to a small system size of a few hundred atoms and a short time scale (≈10–100 ps).[39] As a result, AIMD simulations have to be performed at elevated temperatures (usually >600 K) and can only be performed on materials with high ionic conductivity. AIMD simulations and NEB calculations are highly complementary for studying diffusional properties.

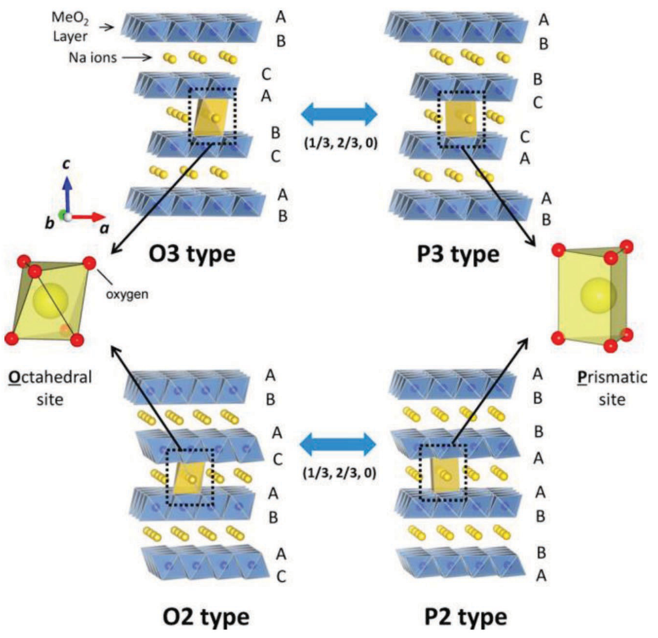

Figure 1. Crystal structures of O3-, P3-, O2-, and P2-type $NaMO_2$. The phase transition of O3-P3 and P2-O2 $NaMO_2$ can be achieved by the gliding of MO_6 layers. Reproduced with permission.[5] Copyright 2014, American Chemical Society.

3. Positive Electrode Materials

There is a strong need for developing high energy density cathode materials for NIBs. Many NIB cathode materials still show poorer performances than LIBs and significant degradation over electrochemical cycling.[82] The understanding of electrochemical sodiation and desodiation processes in NIB cathode materials is crucial for achieving good battery performance compared to LIBs.[83] Here, we review the computational studies of layered oxides (Section 3.1), polyanion compounds (Section 3.2), and organic compounds (Section 3.3) as NIB cathode materials for understanding materials mechanisms regarding the structure, Na ordering, Na^+ diffusion, and phase transformation.

3.1. Layered Oxides $NaMO_2$

Na-ion intercalating transition-metal (TM) oxides $NaMO_2$ with layered structures have attracted great interest as cathode materials for NIBs thanks to their high reversible capacity.[20,84,85] In contrast to the limited choices of TM elements in Li layered oxides $LiMO_2$ (M = Co and Ni),[12–14] reversible Na intercalation was observed in a range of layered TM oxides $NaMO_2$ (M = Ti,[19] V,[86] Cr,[13,18] Mn,[17] Fe,[15] Co,[16] and Ni[18]). In addition, Na_xMO_2 compounds exhibit more types of layered structures, which are denoted as O3, O2, P2, P3, T1, etc., by Delmas et al.,[87] where the letter P, O, or T denotes the prismatic, octahedral, or tetrahedral coordination, respectively, of the alkaline ions (Na or Li) and the number represents the repeating period of MO_6 layers (**Figure 1**). The phase transformation between O3 and P3 (O3–P3) and between P2 and O2 (P2–O2) in $NaMO_2$ can happen through the gliding of MO_6 layers without breaking M—O bonds (Figure 1). In LIBs, the high-performance layered oxide cathodes, such as $LiCoO_2$[88] and $Li(NiMnCo)_{1/3}O_2$,[89] are O3 structures and have simple phase evolution pathways during electrochemical cycling. In contrast, layered $NaMO_2$ compounds in O3, P2, or P3 structures exhibit a variety of Na orderings at different Na concentrations and a number of phase transitions leading to multiple voltage steps during the electrochemical cycling.[34,35] In addition, the layered oxides with different TMs or mixed-TMs also exhibit different Na orderings and stable intermediate phases, leading to different voltage profiles during electrochemical cycling.[6,90,91] Different Na orderings also affect the kinetics of Na^+ diffusion dynamics and phase transitions during electrochemical cycling, and hence significantly impact the electrochemical performances of these cathode materials in NIBs.[10,86,91] By supplementing experimental characterization, computational studies provide crucial knowledge and unique insights about the energies, ionic diffusion, and defects in different structures for the understanding of the cycling mechanisms in these materials. In Section 3.1, we review the recent computational studies on two major types of layered TM oxide cathodes, namely, O3-$NaMO_2$ (Section 3.1.1) and P2-$NaMO_2$ (Section 3.1.2).

3.1.1. O3-Type Layered $NaMO_2$

Structure and Ordering: O3-$NaMO_2$ (M = Ti, V, Cr, Mn, Fe, Co, Ni, or their combinations) provides Na intercalation with high reversible capacity, as a promising candidate for rechargeable NIBs.[20] The structure of O3-$NaMO_2$ contains alternatively stacking slabs of NaO_6 octahedra and MO_6 octahedra with an ABCABC stacking of the oxygen layers (Figure 1). The O3 $NaMO_2$ structure is the same as $LiCoO_2$ widely used in commercial LIBs.[83]

Toumar et al.[37] performed GGA+U calculations to identify ground-state Na orderings in O3 Na_xMO_2 as a function of Na concentrations x for seven TM systems (M = Ti, V, Cr, Mn, Fe, Co, Ni). The convex hull of the formation energies of O3 Na_xCrO_2 is shown in **Figure 2**a. Eighteen Na-vacancy orderings (Figure 2b) were identified as possible ground-state orderings for these Na_xMO_2 systems. The electrostatic interaction among Na ions was found to significantly affect the Na-vacancy ordering. Some ground-state Na orderings, especially at $x \le 1/4$, have relatively homogeneous distributions of Na and vacancies (Figure 2b-a–c), in order to minimize repulsive electrostatic interaction. The clustering tendency of Na ions is observed at high Na concentrations (e.g., Figure 2b-m,n,p). This clustering may be caused by the M^{3+}/M^{4+} charge ordering of TM sublattice and the elastic strain induced by the Na ions in the layers.[37,92]

For each TM system, the preferred Na-vacancy orderings affect the phase transition pathway and performances during electrochemical cycling.[37,86] While all seven TM systems have the same Na ordering at $x = 1/2$ (Figure 2b-g) as the stable ground state in consistent with the characterization by Didier et al.[93] in $Na_{1/2}VO_2$, different TMs systems exhibit a significant variation of the ground-state orderings at different Na concentrations (Figure 2c). In particular, computational and experimental studies[37,45,94] have discovered a highly distinctive ground-state

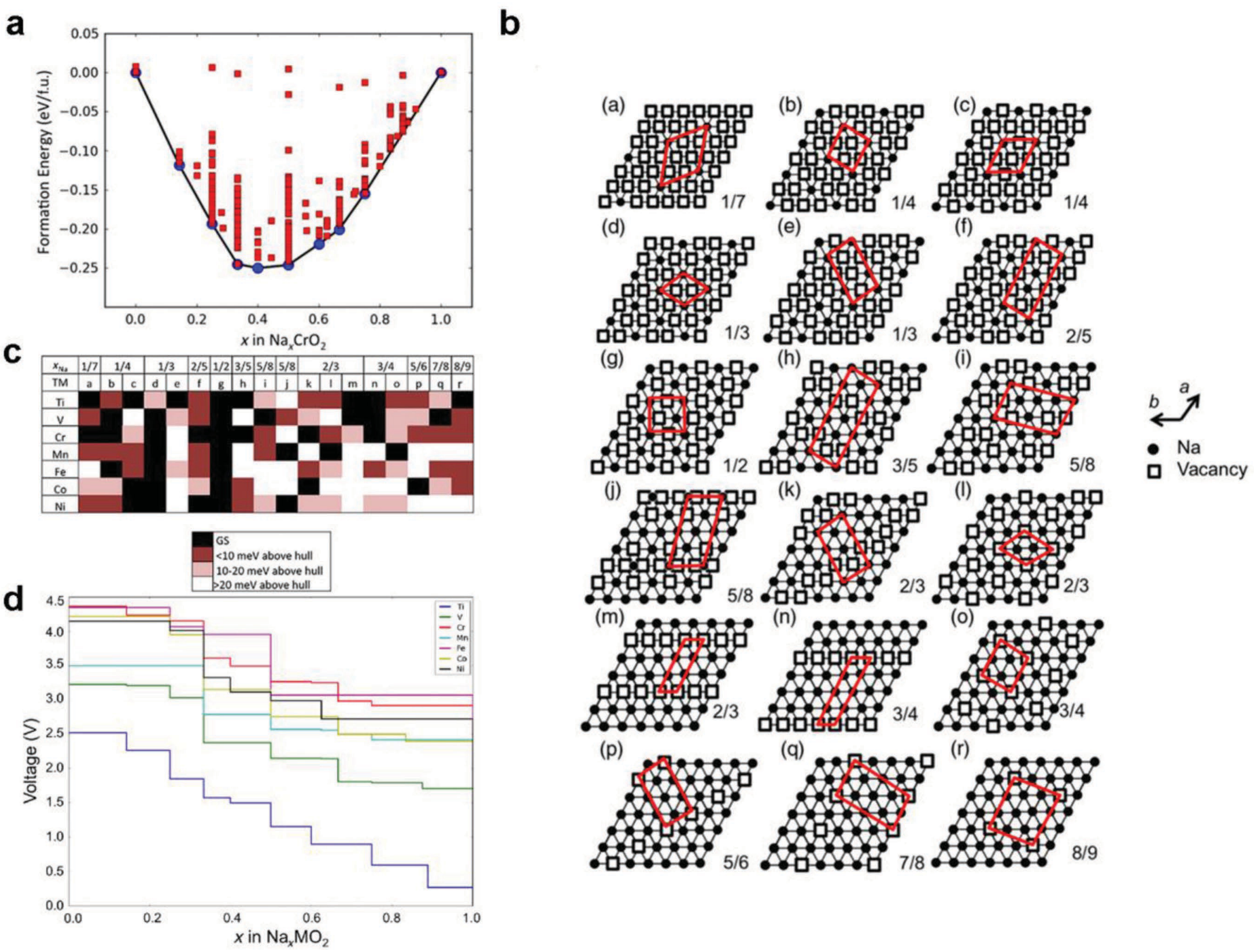

Figure 2. a) Convex energy hull of Na-vacancy orderings in O3 Na$_x$CrO$_2$. b) Low-energy Na-vacancy orderings at different Na concentrations in O3 Na$_x$MO$_2$. c) Energy above the hull of the low-energy Na-vacancy orderings (in (b)) for O3 Na$_x$MO$_2$ with different transition metal M = Ti, V, Cr, Mn, Fe, Co, Ni. d) Computed voltage curves for O3 Na$_x$MO$_2$ (M = Ti, V, Cr, Mn, Fe, Co, and Ni) referenced to Na/Na$^+$. Reproduced with permission.[37] Copyright 2015, American Physical Society.

ordering of Na$_{5/8}$MnO$_2$ and Na$_{5/8}$NiO$_2$ (Figure 2b-j), where Na ions are relaxed into distorted octahedral sites from the original octahedral sites under the strong Jahn–Teller effects of Ni^{3+} and Mn^{3+}. In Na$_x$TiO$_2$ and Na$_x$CrO$_2$ systems, many of the non-ground-state orderings have energies close to the energy convex hull (Figure 2c). This degeneracy of various Na-ordering phases in Ti and Cr systems may lead to Na disordering and facile kinetics during electrochemical cycling, compared to the Fe, Co and Ni systems with distinctive, non-degenerate orderings.[37]

In addition to Na-vacancy orderings within a single Na layer (Figure 2b), the different stacking of Na patterns in adjacent layers also affect the energy of the Na$_x$MO$_2$ structures.[37] The interactions among Na interlayers may be complicated by the charge ordering of TM with different valence states, such as M^{3+} and M^{4+}, as previously shown in Na$_x$CoO$_2$[36] and Li$_x$FePO$_4$.[95] Toumar et al.[37] calculated the energies for different Na-layer stacking based on the same single-layer Na patterns, and found that the energy changes as a result of different Na-layer stacking are different with respect to TMs. For example, the energies of Na$_x$CoO$_2$ are significantly affected by the Na-layer stacking, while Na$_x$CrO$_2$ is less affected. In general, the energy variances of different stacking were found to be no more than ≈30 meV per formula unit. Due to the small formation energies of different stacking, different stacking including stacking faults may easily form in most O3 Na$_x$MO$_2$ systems.

The calculated voltage curves (Figure 2d) are obtained from the identified ground-state Na orderings and energy convex hull (Figure 2b,c) for O3-type Na$_x$MO$_2$ with different TM (M = Ti, V, Cr, Mn, Fe, Co, Ni).[37] Many of the calculated voltage profiles (such as Na$_x$VO$_2$ within $1/2 < x < 1$) are in agreement with major voltage plateaus from electrochemical measurements.[93] All seven O3 systems have phase transitions at $x = 1/2$ and $1/3$ with voltage steps of 0.25–0.75 V (Figure 2d), but the phase transitions at other Na concentrations and their voltage steps vary among TMs. The voltage curves of Na$_x$CrO$_2$ and Na$_x$MnO$_2$ span less than 1.5 V from $x = 0$ to $x = 1$, while that of Na$_x$TiO$_2$ spans more than 2 V. It should be noted that the calculated voltage profiles are from the thermodynamic plateaus from 0 K ground state energies, while the voltage curves

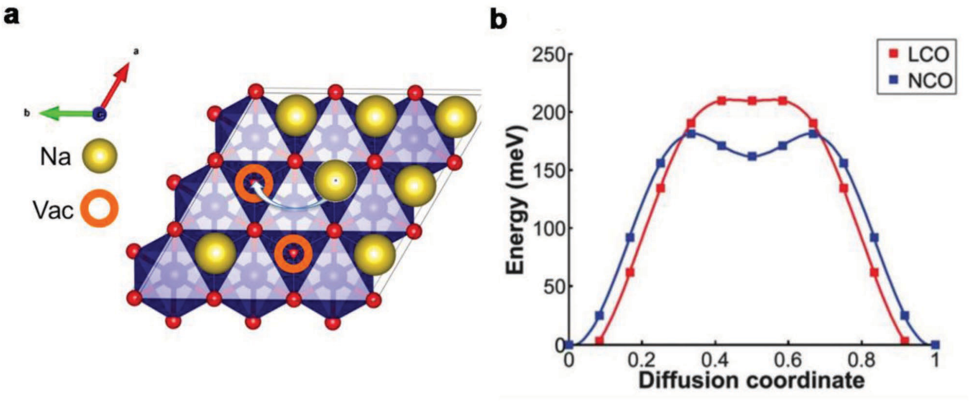

Figure 3. a) Schematic pathway of Na^+ diffusion through divacancy mechanism in O3 Na_xMO_2 (vacancies denoted by empty circles). b) Calculated migration energy barriers of divacancy in O3 Na_xCoO_2 (blue) and Li_xCoO_2 (red). Reproduced with permission.[12] Copyright 2011, Royal Society of Chemistry.

from electrochemical cycling are sensitive to the testing parameters such as the cycling rate,[96,97] etc. Thermodynamic calculations should be compared to the electrochemical tests, such as Galvanostatic intermittent titration technique (GITT), that reflect the equilibrium states of the charge-discharge processes.

Diffusion: Computational studies are performed to reveal the atomistic mechanisms of Na-ion diffusion in O3-Na_xMO_2 cathode materials. Same as in Li_xMO_2, the Na-ion diffusion in Na_xMO_2 is found to happen through a divacancy mechanism (**Figure 3**a),[23,98] where an Na ion migrates through intermediate tetrahedral sites to one of the two vacant octahedral sites (i.e., divacancy). NEB calculations confirmed a low migration barrier of 0.20 eV for the divacancy mechanism of Na^+ migrations in O3-Na_xCoO_2 at the dilute limit of divacancy (Figure 3b).[12] Mo et al.[23] performed AIMD simulations to study Na-ion diffusion at a number of Na concentrations in O3-Na_xCoO_2. The AIMD simulations predicted high Na ionic conductivities ranging from 0.1 to 0.3 mS cm^{-1} at 300 K and low activation energies ranging from 0.28 to 0.24 eV at Na concentrations x of 0.67 and 0.78, respectively. However, the significant drop of Na ionic conductivity was found to occur at $x \approx 1/2$ and $x \approx 1$ in the AIMD simulations. This concentration dependence of ionic conductivity is consistent with previous computational modeling of Li^+ diffusion in Li_xCoO_2.[78] The depletion of mobile Na^+ divacancies at fully sodiated state of $x \approx 1$ may result in the drop of Na^+ conductivity. The drop of Na^+ conductivity at $x \approx 1/2$ in $NaCoO_2$ may be caused by the formation of the Na ordering, as reported in other calculations[37] (Figure 2b-g) and experimental characterizations.[93]

In addition, different TM elements also significantly affect Na-ion diffusion dynamics. Li et al.[99] performed NEB calculations to study Na-ion migration energies in different TM systems of O3-$NaMO_2$ (M = V, Cr, Co, and Ni) at the full sodiation level, and found that Co and V systems have the lowest barriers of 0.46 and 0.45 eV, respectively, and that Ni system has the highest barrier of 0.67 eV. Further computation study is still needed to understand the Na-ion diffusion kinetics in mixed TM systems.

Phase Transformation: The phase transformation of layered O3 Li_xMO_2 with M = V,[102] Mn,[103] Ni,[104] and Co[105,106] to the spinel structure has been known as a key degradation mechanism during long-term electrochemical cycling, causing capacity loss, sluggish kinetics, and poor electrochemical performance.[107,108] For layered Na_xMO_2 compounds, spinel transformation is rarely observed, suggesting good stability of Na layered oxide cathodes materials against the notorious degradation mechanism in LIBs.[100] First principles calculations are performed to study the energies of spinel and layered phases in Li_xMO_2 and Na_xMO_2. As identified by Reed et al.,[109] a critical step for the spinel phase transformation in layered Li_xMO_2 is the formation of the dumbbell defect consisting of a TM ion and a Li^+ ion simultaneously migrated into the tetrahedral sites in the alkali layer (**Figure 4**a). Kim et al.[100] calculated and compared the formation energies of the dumbbell defects in $Li_{0.5}MO_2$ (Figure 4b) and $Na_{0.5}MO_2$ (Figure 4c) (M = Ti, V, Cr, Mn, Fe, Co, Ni) for comparison. The positive formation energies of dumbbell defects in $Na_{0.5}MO_2$ ranging from 166 to 2200 meV indicate the high energy barriers to nucleate spinel phases in O3 Na_xMO_2. This computation result is consistent with the fact that no sodium spinel structure is reported in the ICSD.[110] In contrast to Na compounds, there is a strong driving force in $Li_{0.5}MO_2$ (M = Ti, V, Mn, Fe) to form dumbbell defects with negative formation energies, in consistent with the common experimental observations of lithium spinel phases.[102–104] In particular, the highest formation energy of 308 meV for the dumbbell defect in $Li_{0.5}CoO_2$ confirms $LiCoO_2$ as a stable layered cathode.[12] The different tendency of Li_xMO_2 and Na_xMO_2 layered materials in the spinel transformation is attributed to the ionic radius difference between Na^+ (r = 102 pm) and Li^+ (r = 76 pm).[111] Na^+ ions with the larger size prefer the octahedral sites and are less favorable at the tetrahedral sites, while Li^+ ions may be coordinated by either four or six oxygen ions.

The end member of the electrochemical deintercalation process of Na_xMO_2 is MO_2 in O1 structure,[112,113] and the phase transformation to O1 is not reversible.[112,113] While the spinel transformation is uncommon, O3-$NaMO_2$ layered materials including Na_xCrO_2, Na_xCoO_2, and Na_xNiO_2 were observed to transform into P3 layered structures during electrochemical cycling (Figure 1).[16,18] This O3–P3 transformation is rare in Li layered oxides.[100] The phase transformation from O3 to P3 does not break any M—O bonds and can take place by gliding the

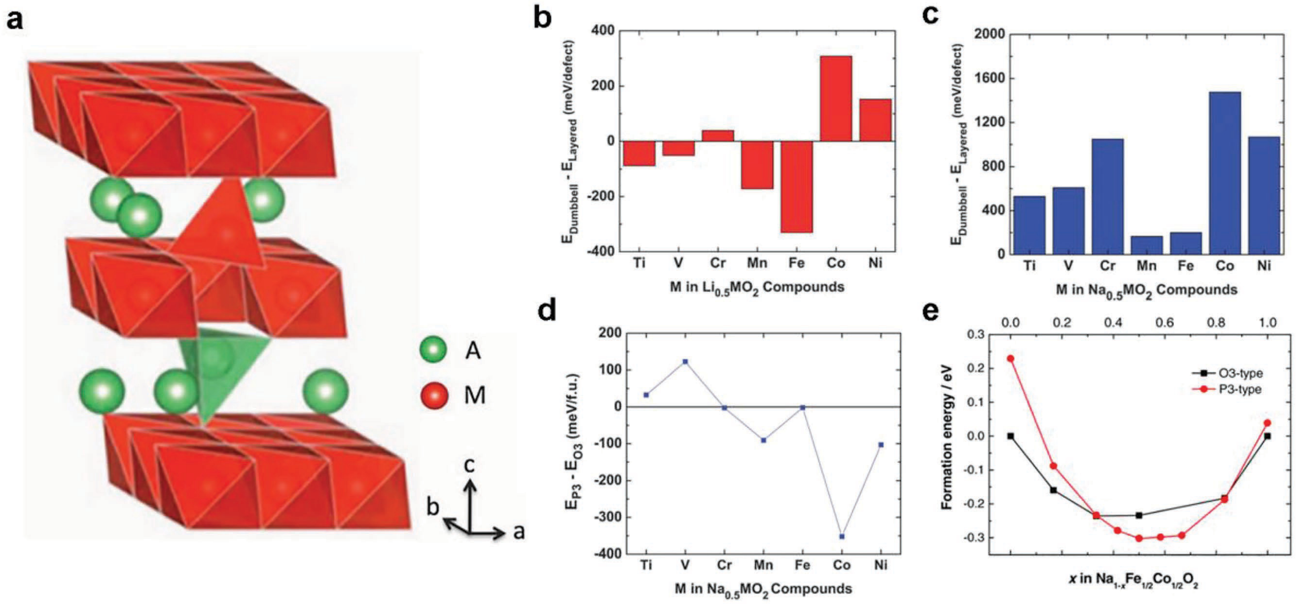

Figure 4. a) Dumbbell defects of a TM ion M and an alkali ion migrated to the tetrahedral sites in the alkali-ion layer. b) Formation energies of dumbbell defects for O3 $Li_{0.5}MO_2$ with M = Ti, V, Cr, Mn, Fe, Co, Ni. c) Formation energies of dumbbell defects for O3 $Na_{0.5}MO_2$. d) Energy difference per formula unit between P3 and O3 $Na_{0.5}MO_2$. Reproduced with permission.[100] Copyright 2012, Royal Society of Chemistry. e) Formation energies of O3 and P3 $Na_{1-x}Fe_{1/2}Co_{1/2}O_2$ as a function of x. Reproduced with permission.[101] Copyright 2016, Wiley-VCH.

TM-oxide layers within the *ab* plane (Figure 1).[100] To evaluate the driving force for the O3–P3 transformation, Kim et al.[100] calculated the energy differences between O3 and P3 phases in $Na_{0.5}MO_2$ (Figure 4d). $Na_{0.5}MO_2$ with M = Mn, Co, Ni are energetically favorable in P3 structures, while $Na_{0.5}TiO_2$ and $Na_{0.5}VO_2$ energetically favor the layered O3 structure. These computation results were consistent with the experimental facts that Na_xVO_2 maintains the O3 structure in shallow charging[86] and that the O3−P3 phase transformation occurs in Na_xCoO_2, Na_xCrO_2, and Na_xNiO_2.[16,18] In addition, the energy preference of O3 versus P3 is a function of Na concentrations x. Kubota et al.[101] investigated the structural evolution of $Na_{1-x}(Fe_{0.5}Co_{0.5})O_2$ using combined experimental analyses and DFT computations (Figure 4e). The computation results showed that P3 is energetically favorable at $0.3 < x < 0.8$, while O3 is favored at $x > 0.8$ and $x < 0.3$ (Figure 4e). The computation results agree with in situ X-ray diffraction (XRD) characterizations in the same study.[101] While one may expect the gliding of TM-oxide layers in O3–P3 transition to be reversible, stacking faults, dislocations and cracks may form during the phase transition and mechanically damage the particles.[113,114] Since the tendency for O3–P3 phase transformation varies greatly among different TMs, optimizing the TM combination to mitigate the O3–P3 phase transition may be a promising material design direction, and computational studies may examine a large number of potential TM combinations in a high-throughput fashion to accelerate this process.

3.1.2. P2-Type Layered $NaMO_2$

Structure and Ordering: In addition to O3 layered structure, P2 layered Na_xMO_2 is another promising class of layered oxide cathode materials for NIBs with high reversible capacity[7] and good structural stability in a wide range of Na concentrations.[35,115] In P2 structure, Na ions reside on two prismatic sites (**Figure 5**), i.e., Na1 and Na2 sites, which are different from the octahedral sites in O3 structure (Figure 1). The NaO_6 prism of the Na1 site shares faces with MO_6 octahedra right above and below, and the prism of the Na2 site shares edges with the MO_6 octahedra (Figure 5). These distinctive Na sites in P2 and O3 structures lead to highly different Na orderings, energies, and Na-ion diffusion, as revealed by computational studies.

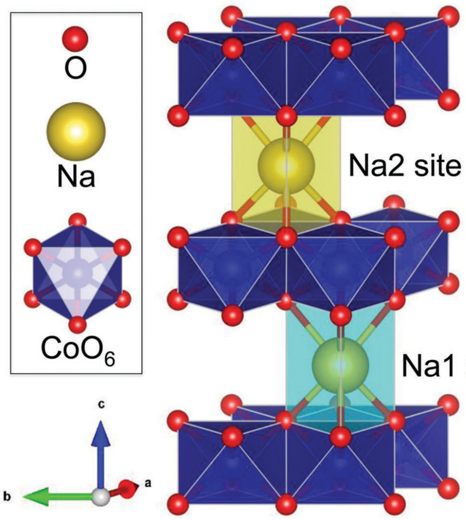

Figure 5. Crystal structure of P2 Na_xCoO_2 with prismatic Na1 and Na2 sites illustrated. Reproduced with permission.[23] Copyright 2014, American Chemical Society..

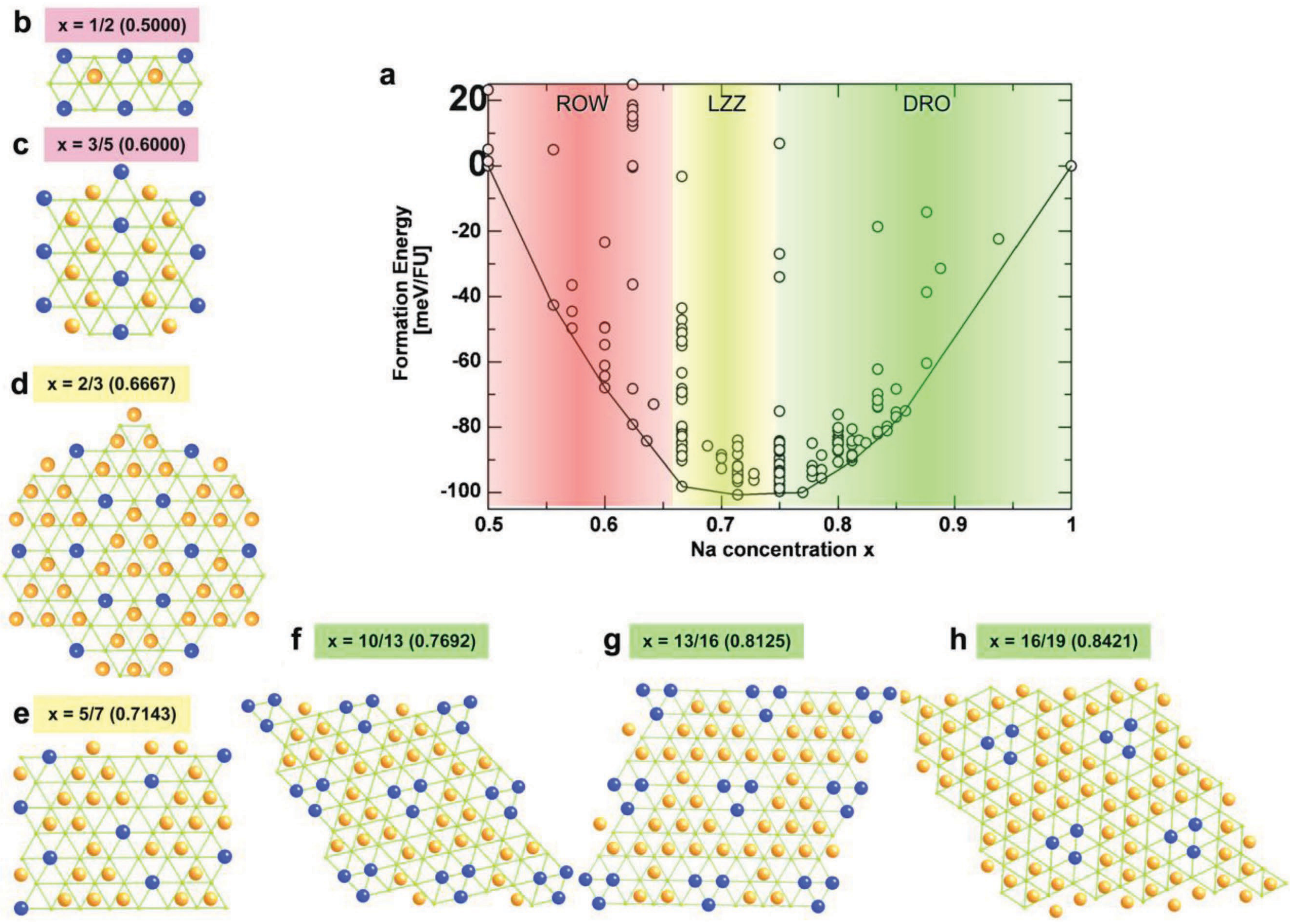

Figure 6. Ground-state Na-vacancy orderings of P2 Na_xCoO_2 ($0.5 \leq x \leq 1$) based on GGA computation (blue: Na1; orange: Na2). The Na orderings were classified into rows (ROW), large zigzag (LLZ), and droplet (DRO) patterns. Reproduced with permission.[43] Copyright 2008, American Institute of Physics.

Given the complexity of two distinct Na sites in P2 Na_xMO_2, understanding Na-vacancy orderings at various Na concentrations is an important research topic for computational investigations. Meng et al.[43] identified the ground-state orderings of Na_xCoO_2 ($0.5 \leq x \leq 1$) using the cluster expansion method fitted to GGA energies. The Na orderings were identified and classified as rows (ROW), large zigzag (LLZ), and droplet (DRO) patterns (**Figure 6**) at different ranges of Na concentration x. The ground-state orderings change from the ROW (Figure 6b,c), to LLZ (Figure 6d,e), and to DRO (Figure 6f–h) patterns as the Na concentration x increases from 0.5 to 1.0. The formation of different ground-state patterns is attributed to the balance between site energies (as the Na1 site is less energetically favorable than the Na2 site) and electrostatic repulsion among Na ions.[43] Other computational studies also identified the Na orderings, such as in $Na_{1/2}CoO_2$[116] (Figure 6b) and DRO patterns (Figure 6f–h),[117] in agreement with the experimental characterizations.[118–120] In addition, the ratios of Na1/Na2 site occupancy were calculated at different Na concentrations x in Na_xCoO_2, and were in qualitative agreement with experimental characterizations.[118,121–123] Na orderings in P2 exhibit strong energy degeneracy at certain concentrations. In particular, many Na orderings in $Na_{0.75}CoO_2$ have similar energies, as shown by the computation of Meng et al.[43] (Figure 6a). These orderings are investigated and confirmed by many computational and experimental studies.[43,116,120,124,125] Given the small energy differences of <20 meV per formula unit among those Na orderings in $Na_{0.75}CoO_2$, different structures may be observed at finite temperatures during electrochemical cycling, as observed in different studies.[36]

Similar to the mixed-TM layered oxides in LIBs, P2 $Na_xM_yM'_{1-y}O_2$ with two or more mixed-TMs have been commonly employed to improve the electrochemical performance in battery cycling.[7,10,90,126,127] Zheng et al.[38] performed DFT calculations in GGA and GGA+U to study the effect of Co–Mn mixing on Na orderings in P2 $Na_xCo_{1-y}Mn_yO_2$. From GGA energy calculations, six ground-state Na orderings were identified in mixed-TM $Na_xCo_{2/3}Mn_{1/3}O_2$ and $Na_xCo_{1/3}Mn_{2/3}O_2$, whereas single-TM Na_xCoO_2 has eight ground-state orderings (**Figure 7**a). These computation results suggest that TM mixing suppresses the Na-vacancy ordering, in agreement with the experimental observations about the suppressed Na ordering in Co–Mn,[91] Co–Mn–Fe,[10] Co–Mn–Ni,[128] and other TM mixing systems. As a result of fewer ground-state orderings, the calculated voltage profile of TM-mixed $Na_xCo_{2/3}Mn_{1/3}O_2$ shows fewer voltages steps than single-TM Na_xCoO_2, in agreement

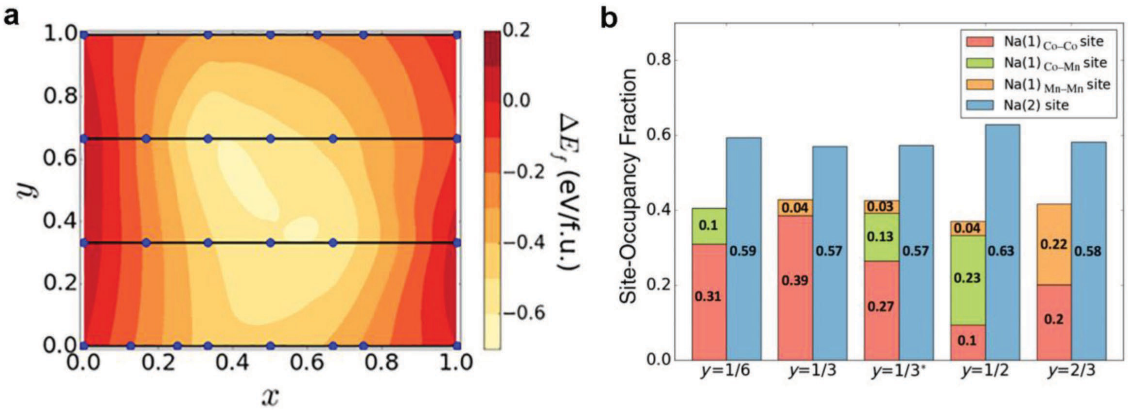

Figure 7. a) Stability diagram of P2 $Na_xCo_{1-y}Mn_yO_2$ described by the formation energy with respect to the fully sodiated and desodiated compounds based on GGA calculations. b) Fraction of Na-ion site occupancy in P2 $Na_{1/2}Co_{1-y}Mn_yO_2$ from AIMD simulations. Reproduced with permission.[38] Copyright 2017, American Physical Society.

with the experiments.[91] In addition, the calculations by Zheng et al.[38] revealed that the change of the Na-vacancy orderings in mixed-TM compounds was caused by the differences of Na1 site energy facing different TMs. The AIMD simulations of $Na_{1/2}Co_{1-y}Mn_yO_2$ found a higher occupancy of $Na1_{Co\text{-}Co}$ site sharing faces with two CoO_6 octahedra than that of $Na1_{Mn–Mn}$ site at Mn concentration y from 1/6 to 1/2 (Figure 7b). Therefore, Mn substitution increases the site energy of the Na1 site facing Mn. In addition to Na orderings and voltage profiles, TM mixing also impacts the Na^+ diffusion[38] as reviewed in the next subsection, significantly affecting the electrochemical performance of NIBs.

Diffusion: P2 $NaMO_2$ cathode materials have good reversibility and excellent rate performance in many experimental studies.[7,129] While the alkali-ion diffusion mechanism is relatively well understood in O3 structures,[98] the Na^+ diffusion mechanism in P2 $NaMO_2$ is complicated by the Na sublattice with two Na sites, Na1 and Na2, and the complex Na orderings at different Na concentrations. Mo et al.[23] performed AIMD simulations to study Na^+ diffusion mechanism in P2 Na_xCoO_2. The AIMD simulations predicted fast Na^+ diffusion in Na_xCoO_2 over a wide range of Na concentrations, suggesting P2 layered oxides are fast Na-ion conductors.[23] High Na^+ conductivities of 4–6 mS cm^{-1} at 300 K and low activation energy of 0.2 eV were reported at $x = 0.56$ and 0.69 from AIMD simulations (**Figure 8**a). The Na^+ conductivity drops to 0.1 mS cm^{-1} at 300 K as the Na concentration increases to $x = 0.75$, and further drops significantly at the full sodiation level $x \approx 1$. This concentration dependence of Na^+ diffusion from AIMD simulations is consistent with the experimental results by Shibata et al.[130] According to the AIMD simulations, Na^+ diffusion kinetics in P2 structure outperforms that in O3 structure (Figure 8a), confirming the superior rate performance widely observed in many P2 systems.[7,129] In addition, the joint DFT and experimental study by Katcho et al.[131] also reported higher Na^+ mobility in P2 than O3 in $Na_{2/3}Fe_{2/3}Mn_{1/3}O_2$. The experimentally measured diffusivity of Na^+ in P2 Na_xCoO_2 is higher than that of Li_xCoO_2.[132] Therefore, the outstanding rate capability of P2 structures originated from the superior Na^+ diffusion kinetics is a major advantage of P2 structures over O3 structures.

Using AIMD simulation, Mo et al.[23] revealed the Na^+ diffusion mechanism in P2 Na_xCoO_2. By tracking Na^+ trajectory during AIMD simulations, they found that Na ions hop between nearest-neighbor Na1 and Na2 sites forming a 2D honeycomb diffusion network (Figure 8c). To understand the details of Na^+ hops in P2, Mo et al.[23] examined the changes of local Na coordination before and after Na^+ hops during AIMD simulations, and characterized each Na^+ hop as the local Na coordination changes (Δc_2, Δc_3), where Δc_2 and Δc_3 refer to the changes in second- and third-nearest coordination number, respectively. While Na^+ hops in P2 structure were observed to be highly diverse, a few hopping modes such as (+2, −4), (−2, +4), (+1, −2), and (−1, +2) were identified as the most frequent hopping modes in $Na_{0.56}CoO_2$. The migration barriers of all these hops observed from AIMD simulations were evaluated using NEB methods. In particular, (+2, −4) hops (Figure 8d) exhibit the highest activation energies of 0.16–0.20 eV (Figure 8b), and are likely the rate-limiting steps for Na^+ migration in P2 $Na_{0.56}CoO_2$. The high activation energies of (+2, −4) hops are attributed to the strong Na-Na electrostatic repulsion caused by the increase of the second coordination number. The strong electrostatic repulsions among Na ions significantly impact Na ordering and Na^+ migration in P2 Na_xCoO_2, and cause the diffusivity drop at high Na concentrations.[23] These computation results suggest that mixing TMs to disorder Na sublattice is a promising strategy to enhance Na^+ diffusion in P2 Na_xMO_2 and to design electrode materials with high rates of electrochemical cycling.

Using AIMD simulations, Zheng et al.[38] further investigated the effect of TM mixing on Na^+ diffusion in P2 $Na_{1/2}Co_{1-y}Mn_yO_2$. The Na ions probability density distribution from AIMD simulations showed preferred Na^+ diffusion via the $Na1_{Co–Co}$ sites in $Na_{1/2}Co_{2/3}Mn_{1/3}O_2$ and $Na_{1/2}Co_{1/2}Mn_{1/2}O_2$ (Figure 8e,f). The preference of Na^+ diffusion via $Na1_{Co–Co}$ over $Na1_{Mn–Mn}$ sites was attributed to the increased site energies of $Na1_{Mn–Mn}$ sharing faces with two Mn ions (as discussed in Section 3.1.2).[38] The increased site energies of $Na1_{Mn–Mn}$ led to higher barriers for Na^+ hopping through these sites. The NEB calculations found a low energy barrier of 76 meV for Na^+ migration through $Na1_{Co–Co}$ and a higher energy barrier of 100 meV or 90 meV for the Na^+ migration

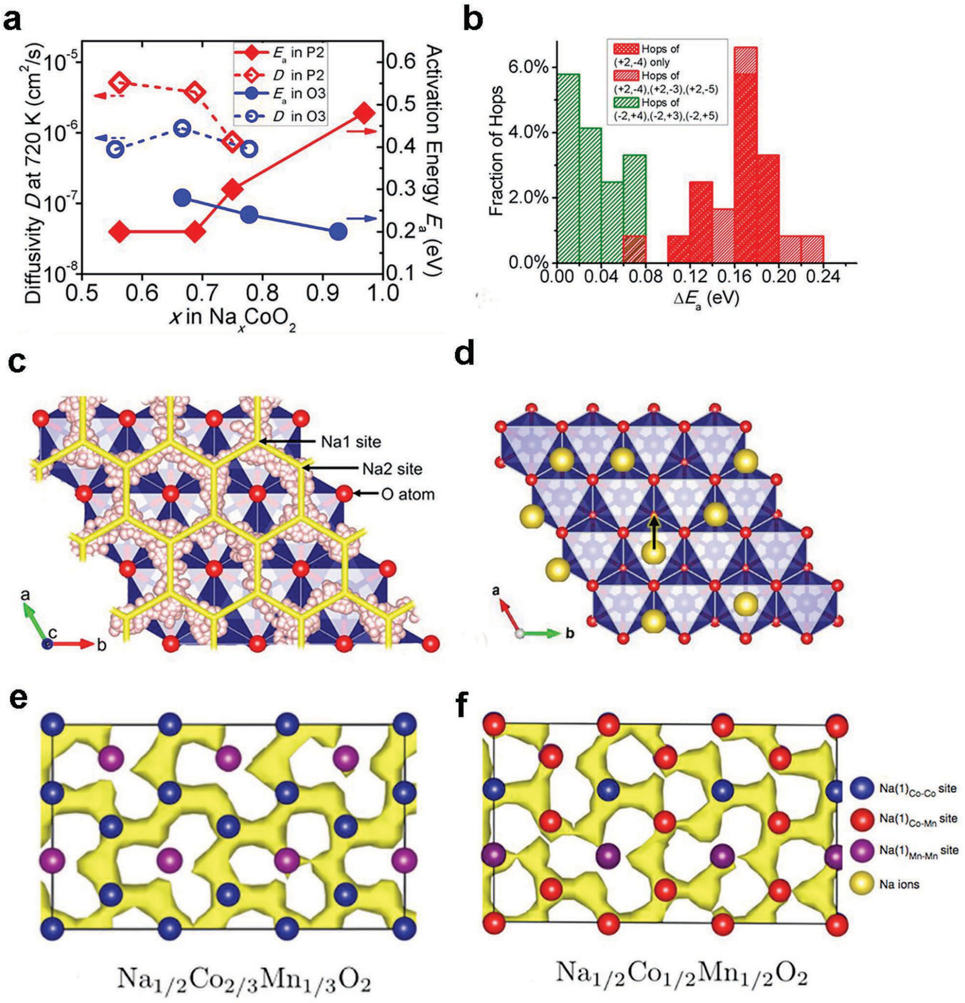

$Na_{1/2}Co_{2/3}Mn_{1/3}O_2$ $Na_{1/2}Co_{1/2}Mn_{1/2}O_2$

Figure 8. a) Na^+ diffusivity and activation energy for P2 and O3 Na_xCoO_2 from AIMD simulations at 720 K and NEB calculations. b) The occurrence fraction of (+2, −4) hops from AIMD simulations and corresponding migration energies calculated by NEB calculations. c) Na^+ trajectory (white spheres) from AIMD simulations and Na^+ diffusion pathways (yellow lines). d) One Na^+ hop observed in AIMD simulations classified as (+2, −4). Reproduced with permission.[23] Copyright 2014, American Chemical Society. Na ions probability density distribution in e) $Na_{1/2}Co_{2/3}Mn_{1/3}O_2$ and f) $Na_{1/2}Co_{1/2}Mn_{1/2}O_2$ from AIMD simulations. Reproduced with permission.[38] Copyright 2017, American Physical Society.

through $Na1_{Mn-Mn}$ or $Na1_{Co-Mn}$, respectively.[38] Thus, Mn substitution has a detrimental effect on Na^+ diffusion. Other TMs such as Fe and Ni were predicted to decrease the migration barriers through Na1 sites and to facilitate Na^+ diffusion.[38] These computation results provide important guidance for rationally choosing TM mixing and tuning compositions to improve the electrochemical performance of P2 cathode materials.

Phase Transformation: In general, the energies of P2, O3, and other layered structures are close. P2 structures are usually stable at an intermediate Na concentration range of $0.4 < x < 0.85$,[8] and O3 structures are more favorable at high Na concentration $0.9 < x < 1$ as observed in materials syntheses.[133] DFT and experimental studies by Katcho et al.[131] report similar stability of P2 and O3. From the energy perspective, it is possible that multiple phases may coexist in different particles or within one particle in the electrode.

Similar to the O3–P3 phase transformation in O3 compounds, P2 cathodes also undergo phase transformation from P2 to O2 during electrochemical cycling.[129] The P2–O2 phase transformations are often not fully reversible and should be suppressed in order to improve reversible capacity. Lee et al.[129] conducted a DFT computation study combined with diffraction experiments to elucidate the P2–O2 transformation mechanism in P2 $Na_x(Ni_{1/3}Mn_{2/3})O_2$. The DFT calculations indicate O2 structures are more energetically favorable than P2 at low Na concentrations, consistent with the experimentally observed phase transformation from P2 to O2 at 4.22 V.[129] In addition, NEB calculations found higher Na^+ migration barriers in O2 structures than those in P2 structures, but the migration barriers are decently low in both P2 and O2 structures, in agreement with high Na^+ diffusivity observed in GITT experiments.[129]

DFT versus DFT+U Calculations: The incorporation of the Hubbard *U* correction[53] into DFT calculations favors the charge localization on TMs forming $M^{3+/4+}$ instead of an averaged valence between 3+ and 4+ due to delocalized charge calculated by the GGA or LDA.[36,38,43,124] However, it is not always straightforward whether the localized charged state or the delocalized charge is more appropriate. In many studies, the properties calculated by GGA were compared with those calculated by GGA+*U*. In the study by Zheng et al.,[38] both GGA and GGA+*U* calculations identified the same ground-state orderings at most Na concentrations except at $x = 1/8$ in Na_xCoO_2. GGA+*U* calculations did not reproduce the experimentally observed ground states at $x = 0.60$, 0.67, 0.71, and 0.77 in Na_xCoO_2.[43] Therefore, DFT calculations without the Hubbard *U* may be more accurate in evaluating ground-state Na ordering.[36,38,43] Hinuma et al.[36] found that the *c* lattice parameter of P2 Na_xCoO_2 calculated by GGA agreed better with the experimental values from the neutron diffraction[121] and that GGA+*U* overestimated the *c* lattice parameter. In addition, Hinuma et al.[36] found that the Na1/Na2 ratios calculated from GGA matched better with experiments than those obtained by GGA+*U*. The GGA+*U* calculations reproduce the Na intercalation voltage better than GGA compared to the experimental voltage values, as demonstrated by the voltage calculations of $Na_xCo_{1-y}Mn_yO_2$[38] and Na_xCoO_2.[36] While GGA without Hubbard *U* better reproduces most properties of Na_xCoO_2 at $0.5 < x < 0.8$,[36,43] GGA+*U* captures the Jahn–Teller effect of Mn^{3+} and may better reproduce the properties of $Na_xCo_{1-y}Mn_yO_2$.[38] There is no simple conclusion regarding whether DFT or DFT+*U* better describes all properties of Na_xMO_2. One needs to perform the calculations using both DFT and DFT+*U* and compare the results to experiments, as in most computational studies.

3.2. Polyanion Compounds

In addition to layered oxide materials, polyanion compounds have been widely investigated as cathode materials for NIBs.[4,5,134] Although heavy polyanion groups limit the specific capacity of these materials, multiple polyanions (e.g., PO_4^{3-}, $P_2O_7^{4-}$, SO_4^{2-}) offer a diverse pool of open-framework crystal structures, and the strong covalent bonding of the polyanions provides robust structural framework during electrochemical cycling.[20,79] In addition, some polyanion systems in particular those with mixed F^- anions may offer higher voltages than layered oxide cathodes.[20] In this section, we review computational studies on phosphates (Section 3.2.1), fluorophosphates (Section 3.2.2), pyrophosphates (Section 3.2.3), sulfates (Section 3.2.4), carbonophosphates (Section 3.2.5), and NASICON (NA Super Ionic CONductor) (Section 3.2.6).

3.2.1. Phosphates $NaMPO_4$ (M = Fe, Mn)

Structure and Ordering: The success of the $LiFePO_4$ cathode for LIBs motivates the study of $NaMPO_4$ (M = Fe or Mn) materials as cathodes for NIBs.[20,136–142] The $NaMPO_4$ compounds have olivine (**Figure 9**a) and maricite structures (Figure 9b). While the olivine structure is more energetically favorable than the maricite structure in $LiFePO_4$,[12] multiple computational studies indicate these two structures have similar energies in $NaMPO_4$,[12,136] and experimental studies indicated maricite is the thermodynamically stable phase.[143–145] However, the maricite phase lacks a good Na^+ diffusion path in the structure (Figure 9b). The electrochemically active olivine $NaMPO_4$ can be obtained by delithiation and subsequent sodiation of olivine $LiMPO_4$.[136] The olivine $NaMPO_4$ structure has a *Pnma* space group and comprises vertex-sharing MO_6 octahedra and PO_4 tetrahedra that share one edge and all vertices with MO_6 octahedra (Figure 9a). The Na sites in olivine $NaMPO_4$ form linear chains parallel to the *b* axis providing open channels for Na ion diffusion along the *b* axis (Figure 9a). $NaFePO_4$ and $NaMnPO_4$ with olivine structures are indeed demonstrated as promising cathode materials with relatively high discharge capacity of ≈150 mA h g^{-1} and good reversibility.[136–142]

Saracibar et al.[135] performed GGA+*U* computations to study the phase evolution and Na orderings of Na_xFePO_4 with different Na concentrations ranging from $x = 0$ to $x = 1$ (Figure 9c). Two ground-state structures, i.e., $Na_{2/3}FePO_4$ and $Na_{5/6}FePO_4$, were identified (Figure 9c), in agreement with previous experimental reports of an intermediate phase $Na_{2/3}FePO_4$ and a phase transition between $FePO_4$ and $Na_{2/3}FePO_4$.[136,139,140,146] In addition, the calculations also found that the Na-vacancy ordering was coupled with the configuration of $Fe^{2+/3+}$ with different oxidation states in Na_xFeO_4 (Figure 9c). Fe^{3+} ions locate close to Na vacancies within the (110) planes, as the Na-vacancy planes tend to increase the separation spacing. Both $Na_{2/3}FePO_4$ and $Na_{5/6}FePO_4$ form $3a3bc$ superstructures resulting from the coupled Na-vacancy and $Fe^{2+/3+}$ charge ordering (Figure 9c). These calculated orderings of Na-vacancy and $Fe^{2+/3+}$ in $Na_{2/3}FePO_4$ are in good agreement with the characterizations.[139,140] The calculated ground-state ordering of $Na_{5/6}FePO_4$ has similar features to $Na_{2/3}FePO_4$, as half of the (110) planes of Na vacancies are filled upon the sodiation of $Na_{2/3}FePO_4$ (Figure 9c). Based on the ground-state ordered structures of Na_xFePO_4, Saracibar et al.[135] calculated the average voltage of Na_xFePO_4 as 3.01 V, in agreement with previous experiments.[136] The calculated voltage plateaus of 3.07 and 2.92 V are in agreement with experimental values of 3.06 and 2.89 V, respectively.[135]

Diffusion: Computations were performed to study Na^+ migration along several possible pathways, such as [010], [001], and [101], in olivine $NaMPO_4$.[12,79,147] The Na^+ migration along [010] channels (**Figure 10**a) was calculated to have the lowest migration energy of 0.28 or 0.38 eV at desodiated or sodiated states of Na_xFePO_4 (Figure 10b), respectively, compared to higher energy barriers of >1.5 eV along [001] and [101].[12,79,147] Therefore, olivine Na_xFePO_4 has the same diffusion mechanism as Li_xFePO_4.[12] The facile diffusion of Na^+ along [010] channels indicates olivine Na_xFePO_4 is mainly a 1D Na-ion conductor. Compared to Li_xFePO_4, Na^+ diffusion in Na_xFePO_4 has a higher migration energy barrier (Figure 10b).

Phase Transformation: Similar to that in $LiFePO_4$,[148] the antisite defects formed by exchanging Na^+ with M cation on neighboring sites are proposed to significantly decrease the electrochemical performance of olivine Na_xFePO_4 by blocking the facile 1D channel along *b* axis.[79] If Na are completely exchanged with M in olivine Na_xMPO_4, the olivine structure would transform into the maricite structure, which has no obvious open channels for low-barrier alkali-ion diffusion (Figure 9b). Tripathi et al.[79] calculated the formation energies of multiple defects in olivine $NaMPO_4$ using classical interatomic potentials. The formation of the Frenkel and Schottky defects is calculated to have high formation energies, similar to those in $LiFePO_4$.[149,150] In contrast, antisite defects in

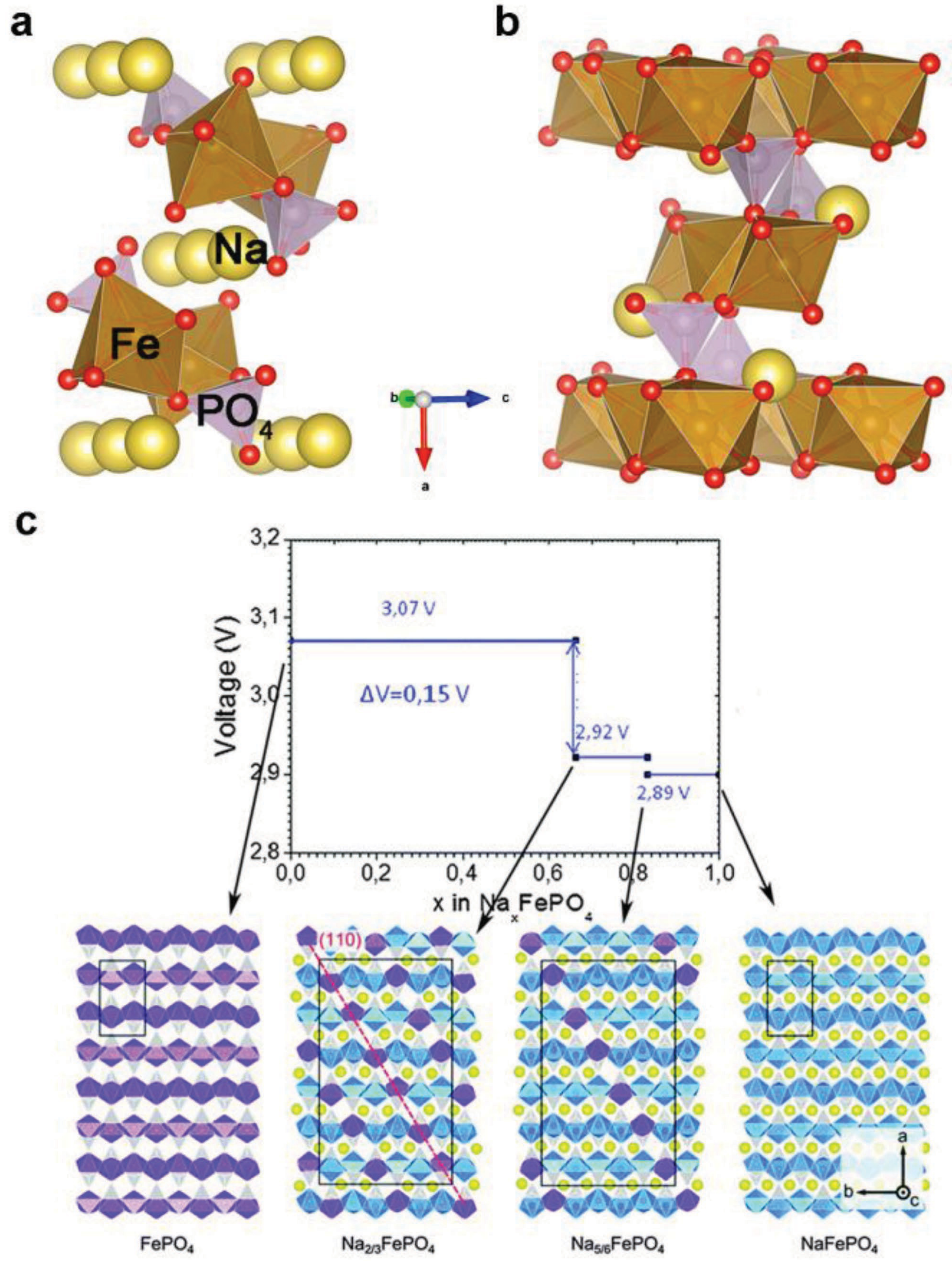

Figure 9. Crystal structures of a) olivine and b) maricite $NaFePO_4$. c) Computed voltage profiles referenced to Na/Na^+ and corresponding ground-state structures of Na_xFePO_4 (Fe^{2+}: blue; Fe^{3+}: purple; Na^+: yellow; $PO_4{}^{3-}$: gray). The dashed red line in $Na_{2/3}FePO_4$ represents the (110) plane. Reproduced with permission.[135] Copyright 2016, Royal Society of Chemistry.

$NaFePO_4$ or $NaMnPO_4$ are calculated to have significantly lower formation energies of 0.86 or 1.06 eV, respectively. The low formation energies of antisite defects in olivine $NaFePO_4$ are consistent with the experimental result that olivine $NaFePO_4$ readily transforms to the thermodynamically stable maricite phase upon heat treatment.[144] The DFT energies revealed that maricite $NaMPO_4$ has slightly lower energy than the olivine phase,[136] while olivine $LiMPO_4$ was calculated to be stable.[12] Tripathi et al.[79] attributed the site preference of alkali and M ions and the structure preference of maricite versus olivine to the interplay between cation charge and different ion radius. While Li^+ (r = 0.76 Å) and Fe^{2+} (r = 0.78 Å) have similar ionic radii, the larger size Na^+ (r = 1.02 Å) prefers the M site in olivine structure, which has larger space than the alkali-ion site.

3.2.2. Fluorophosphates

Na_2MPO_4F (M = Fe, Mn, Co, Ni): The incorporation of highly electronegative F ions into phosphate-based materials is a promising materials design strategy for high-voltage cathodes in NIBs. A number of fluorophosphates with a general formula

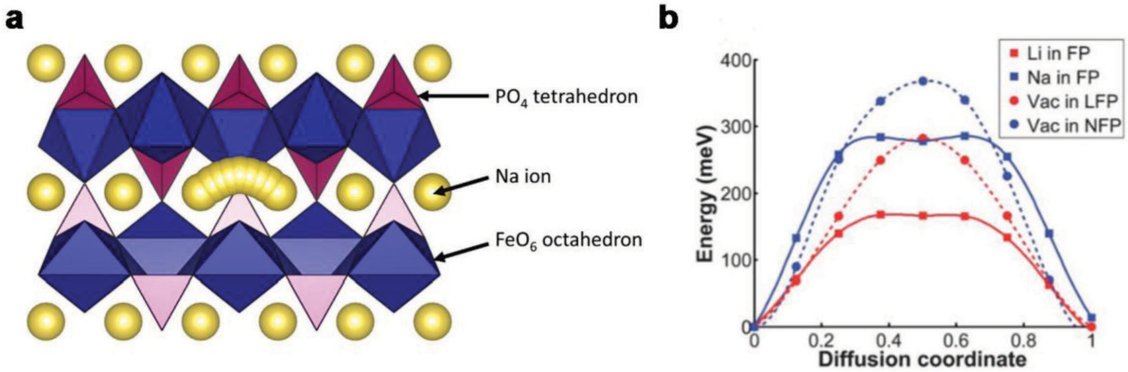

Figure 10. a) Calculated Na^+ migration pathway along [010] channels in olivine $NaFePO_4$. Reproduced with permission.[147] Copyright 2016, Elsevier. b) Calculated Na^+ diffusion barriers in olivine Na_xFePO_4 (blue) and Li_xFePO_4 (red) at $x = 0$ and 1. Reproduced with permission.[12] Copyright 2011, Royal Society of Chemistry.

of Na_2MPO_4F (M = Fe, Mn, Co, Ni) have been reported as promising cathodes.[20,153] For example, Na_2FePO_4F and Na_2MnPO_4F are demonstrated with reversible capabilities of 110 and 178 mA h g^{-1}, respectively.[154,155] Na_2MPO_4F has two polymorph structures the monoclinic structure with $P2_1/c$ space group in Na_2MnPO_4F (**Figure 11**a)[156,157] and the layered orthorhombic structure with *Pbcn* space group in Na_2FePO_4F and Na_2CoPO_4F (Figure 11b).

The increased voltages in fluorophosphates compared to phosphates are quantified and confirmed by computational studies.[152] For the monoclinic Na_2MnPO_4F, which has been tested as a high energy density cathode material,[155,158–160] GGA+U computation[152] indicates an equilibrium sodiation voltage of 3.71 V at $1.5 \leq x \leq 2$ and 3.76 V at $1 \leq x \leq 1.5$, respectively (Figure 11c), in good agreement with the experimental value of 3.75 V.[151,158] DFT calculations[79,152] also quantified that

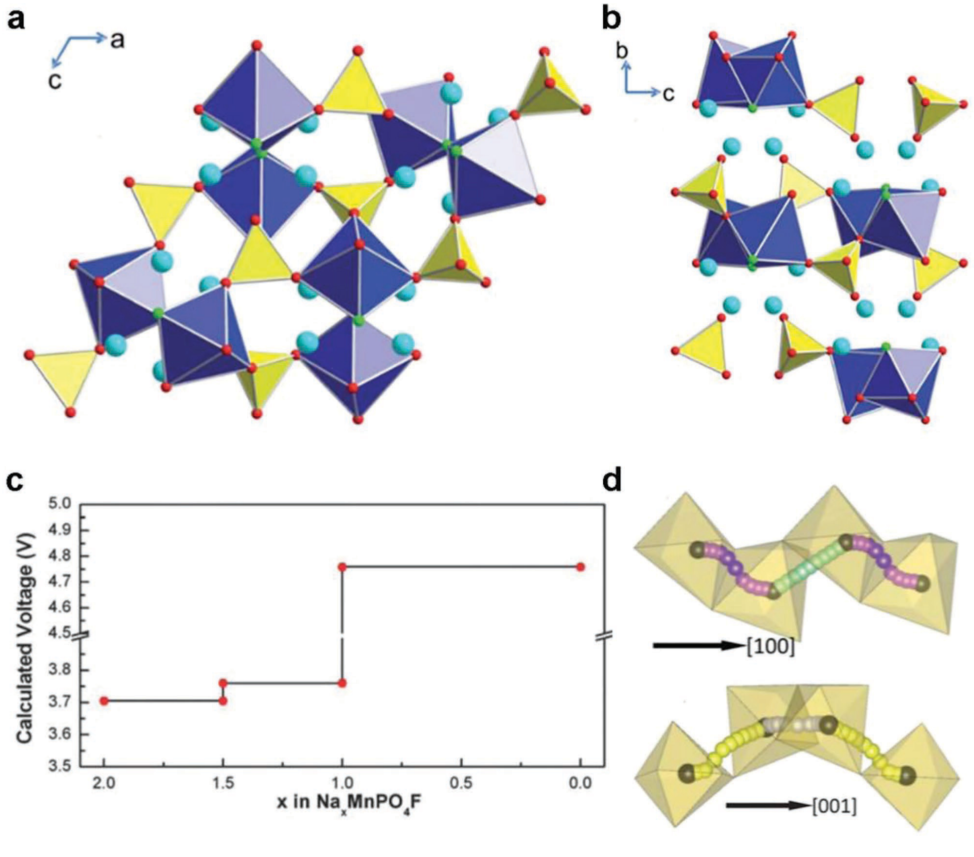

Figure 11. Crystal structures of a) Na_2MnPO_4F with a space group of $P2_1/c$ and b) Na_2FePO_4F with a space group *Pbcn*. Yellow: PO_4 tetrahedra. Blue: MO_4F_2 octahedra; Light blue sphere: Na^+. Reproduced with permission.[151] Copyright 2011, Royal Society of Chemistry. c) Calculated voltage profiles of Na_2MnPO_4F referenced to Na/Na^+. Reproduced with permission.[152] Copyright 2013, The Electrochemical Society. d) Na^+ diffusion pathways in Na_2FePO_4F. Reproduced with permission.[79] Copyright 2013, Royal Society of Chemistry.

the volume expansion of Na_2MnPO_4F or Na_2FePO_4F during sodiation is less than 20%, confirming the robustness of the crystal framework during electrochemical cycling.[20]

Similar to phosphate cathodes, the robust 2D diffusion network consisting of interconnected FeO_4F_2–PO_4 polyhedra (Figure 11b) in Na_2FePO_4F provides facile Na-ion diffusion and good intercalation reversibility.[79,153,161] Tripathi et al.[79] performed calculations based on interatomic potentials to investigate Na^+ diffusion pathways and migration barriers in Na_2FePO_4F. Their results suggest that Na ions migrate in the 2D diffusion network of Na_2FePO_4F along [100] and [001] directions (Figure 11d) with low energy barriers of 0.29 and 0.44 eV, respectively. These low barriers and 2D Na^+ diffusion in Na_2FePO_4F are advantageous compared to the 1D Na^+ diffusion in $NaFePO_4$.[79] In the experiments, Na^+ intercalation and deintercalation from Na_2FePO_4F are observed to be more facile than olivine $NaFePO_4$.[162,163]

$Na_3V_2(PO_4)_2F_3$: V-based fluorophosphate compounds have been investigated as promising cathodes with high voltage, stable cycling performance, and multiple-electron redox from V^{3+} to V^{5+}.[20] $Na_xV_2(PO_4)_2F_3$ was demonstrated to have a reversible capacity of ≈120 mA h g^{-1} (corresponding to $1 \le x \le 3$) and high voltage plateaus at 3.7 and 4.2 V.[164–167] The structure of $Na_3V_2(PO_4)_2F_3$ consists of $V_2O_8F_3$ bioctahedra connected by PO_4 tetrahedra and Na^+ layers lying in the *ab*-plane (**Figure 12**ac).

A combined computation and diffraction study by Shakoor et al.[165] on $Na_{3-x}V_2(PO_4)_2F_3$ suggested a reversible

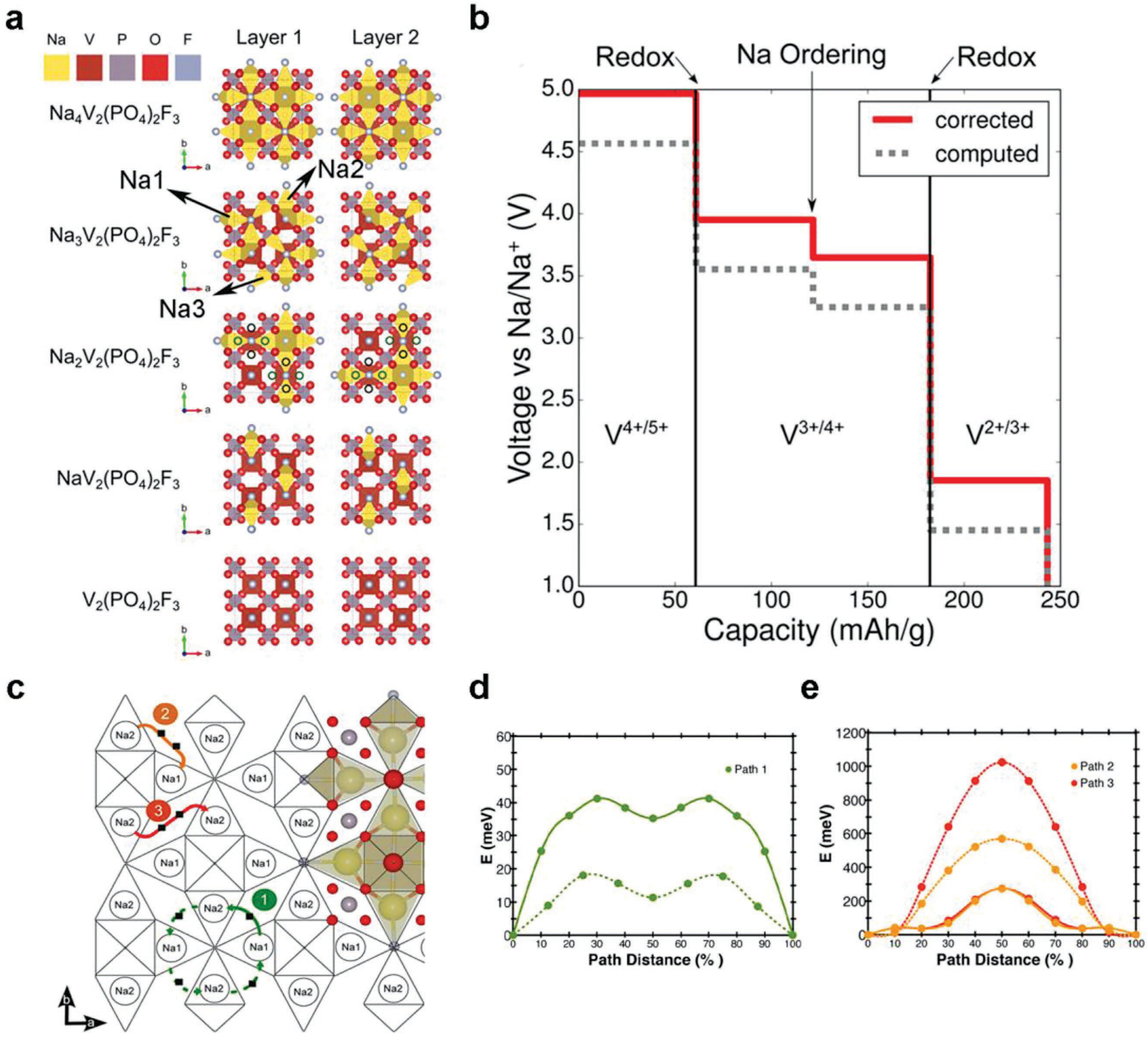

Figure 12. a) Calculated ground-state Na ordering in $Na_xV_2(PO_4)_2F_3$ ($0 \le x \le 4$) unit cell. b) Calculated voltage profile of $Na_xV_2(PO_4)_2F_3$ ($0 \le x \le 4$). Reproduced with permission.[24] Copyright 2016, American Chemical Society. c) Na^+ diffusion pathways within the Na plane in $Na_xV_2(PO_4)_2F_3$. Black dots along paths 2, 3 denote the Na3 sites. d) Migration energies for path 1 at the sodiated (dotted) and desodiated (solid) limits. e) Migration energies for paths 2 and 3 at the sodiated (dotted) and desodiated (solid) limits. Reproduced with permission.[76] Copyright 2015, American Chemical Society.

sodiation/desodiation through a one-phase reaction pathway. Recently, Dacek et al.[24] performed a systematic GGA+U computation study for Na configurations in $Na_3V_2(PO_4)_2F_3$ and revealed detailed knowledge about this structure over a wide range of Na concentrations (Figure 12a). The calculated ground state of $Na_3V_2(PO_4)_2F_3$ has a $Cmc2_1$ space group with an orthorhombic distortion of the a and b lattice parameters ($b/a \approx 1.004$), which is consistent with the experimental characterization ($b/a \approx 1.002$) by Bianchini et al.[168] Na ions occupy Na1 and Na2 sites, which are along the [100] and [010] directions, respectively, from each bioctahedra center, and Na3 sites, which are along the [110] directions from the center of the ring (Figure 12a). These computational results agree with the high-resolution diffraction characterizations[167,168] in contrast to earlier experimental reports that $Na_3V_2(PO_4)_2F_3$ is a tetragonal $P4_2/mnm$ structure with only Na1 and Na2 sites.[164] Dacek et al.[24] also identified Na orderings in desodiated compositions $Na_xV_2(PO_4)_2F_3$ ($0 \le x \le 4$) through DFT computation. The ground-state structures of $Na_2V_2(PO_4)_2F_3$ and $NaV_2(PO_4)_2F_3$ were calculated to have orthorhombic $Cmmm$ and $Cmcm$ space groups (Figure 12a), respectively, with Na ions occupying Na1 and Na2 sites, in consistent with the experiments.[167,168]

In addition, $Na_xV_2(PO_4)_2F_3$ ($0 \le x \le 4$) is calculated to have small decomposition energies of <17 meV per atom at all sodiation levels,[24] suggesting a small thermodynamic driving force for phase decomposition and good structural stability during electrochemical cycling, as observed in the experiments.[165–168] Dacek et al.[24] also investigated phase stabilities of $Na_xV_2(PO_4)_2O_{2y}F_{3-2y}$ ($0 \le y \le 1$) with different O-F mixing ratios. The decomposition energies of $Na_xV_2(PO_4)_2O_{2y}F_{3-2y}$ ($0 \le y \le 1$) with the sodiation level $x \le 3$ are less than 10 meV per atom, suggesting good structural stabilities for the compounds with different O–F mixing ratios. The fully sodiated phase at $x = 4$ becomes substantially more unstable with a decomposition energy of ≈50 meV per atom, suggesting unlikely topotactic sodium insertion into O–F mixed compounds at $x > 3$.

Based on the calculated Na orderings and structures, Dacek et al.[24] further calculated the voltage profile of $Na_xV_2(PO_4)_2F_3$ during sodiation (Figure 12b). The first voltage plateau at $0 \le x \le 1$ associated with the V^{4+}/V^{5+} redox couple is 4.9 V, in good agreement with the experimental value of 5.0 V.[166,169] Such high voltage is above the electrochemical window of typical sodium electrolytes (4.5 V),[170] impeding the electrochemical extraction of all Na ions.[171] In order to address this issue, Xu et al.[169] studied the voltages of $Na_xV_2(PO_4)_2F_3$ with other mixed halogens such as Br and Cl, and discovered that the substitution of $F_{0.5}Br_{0.5}Cl_2$ at the F sites significantly decreases the first voltage plateau to 4.1 V within the electrochemical window of current electrolytes. This computation work suggests tuning anion mixing in polyanion systems to tailor the voltage for improved electrolyte compatibility.

Matts et al.[76] performed NEB calculations to study Na^+ diffusion in $Na_xV_2(PO_4)_2F_3$. They discovered that Na^+ migration occured within the ab plane of $Na_xV_2(PO_4)_2F_3$ through the path 1, 2, and 3 in Figure 12c. The migration energy of path 1 is much lower (≈20–45 meV) than those of path 2 (≈300–600 meV) and path 3 (≈300–1100 meV) (Figure 12de). Dacek et al.[24] performed AIMD simulations in $Na_xV_2(PO_4)_2F_3$ and obtained the activation energies of 155–811 meV, in agreement with NEB calculations.[76] The activation energies of Na^+ diffusion (353–811 meV) are significantly higher in the ordered structures at $x = 1, 2, 3$ than those (155–726 meV) in disordered structures with fractional Na concentrations.[24] In experiments, Liu et al.[172] observed that Na^+ diffusivity droped dramatically near $x = 1$. Given the relative low migration barrier at $x = 1$ from NEB calculations, Dacek et al.[24] attributed the drop of Na^+ diffusivity in the ordered structures ($x = 1, 2, 3$) to the lack of mobile carriers, and proposed to increase Na^+ conductivity through disordering Na sublattice by mixing TMs or by disordering anion sublattice. In addition, the TM mixing may suppress Na-vacancy ordering and may decrease the high voltage (≈4.9 V) to extract sodium, facilitating Na^+ diffusion kinetics in the compositions at $x = 1, 2, 3$.

3.2.3. Pyrophosphates $Na_2MP_2O_7$ (M = Fe, Mn)

Pyrophosphates $Na_2MP_2O_7$ (M = Fe, Mn) represent another type of polyanion cathode materials for NIBs.[173,174] Though the theoretical capacity of pyrophosphates is lower than those of phosphates and fluorophosphates,[20] pyrophosphates have good stability and open frameworks.[175–177] While these pyrophosphate materials with different TMs adopt different crystal structures, many of these structures exhibit open diffusion channels for Na^+ diffusion during electrochemical cycling.[20] In this section, we will review the representative pyrophosphate systems, $Na_2FeP_2O_7$, $Na_2MnP_2O_7$, and $Na_4Mn_3(PO_4)_2(P_2O_7)$.

Structure and Ordering: DFT computation studies identified the intermediate phases during sodium intercalation and deintercalation.[176–178,180] For $Na_xFeP_2O_7$ over $1 < x < 2$, DFT calculations[178] suggested a single-phase reaction around 2.5 V and a series of two-phase reactions in the voltage range of 3.0–3.25 V, consistent with experimental characterizations.[178] The 2.5 V plateau corresponds to the first Na extracted from the Na1 site, and the 3 V plateau corresponds to Na ions extracted from the Na3–Na8 sites (**Figure 13**a). A joint computational and experimental study[176] on $Na_2MnP_2O_7$ also presented similar intermediate phases with one single-phase reaction at 3.32 V and three consecutive two-phase reactions at 3.66, 3.98, and 4.15 V. In addition, Park et al.[176] argued that $Na_2MnP_2O_7$ had better stability than $Li_2MnP_2O_7$ because of the Jahn-Taller distortion allowing better electrochemical performance of the Na compounds. In $Na_4Mn_3(PO_4)_2(P_2O_7)$, DFT calculations[180] predicted a single-phase reaction for extracting one Na from the structure, and then a two-phase reaction for further Na extraction, in agreement with the experimental observations.[180] The computation[180] found the intermediate β phase was not a ground state in the calculated energy convex hull and might be kinetically formed during electrochemical cycling.

Diffusion: Kim et al.[178] studied Na^+ diffusion in the intermediate phases of $Na_xFeP_2O_7$ formed during desodiation (Figure 13a). At $x = 1$, the Na^+ migration along the [011] channel has an energy barrier of 0.48 eV. For other intermediate phases corresponding to the plateaus at ≈3 V, Na^+ migrations through the 1D channels and 2D pathways have the barriers below 0.54 eV (Figure 13a).

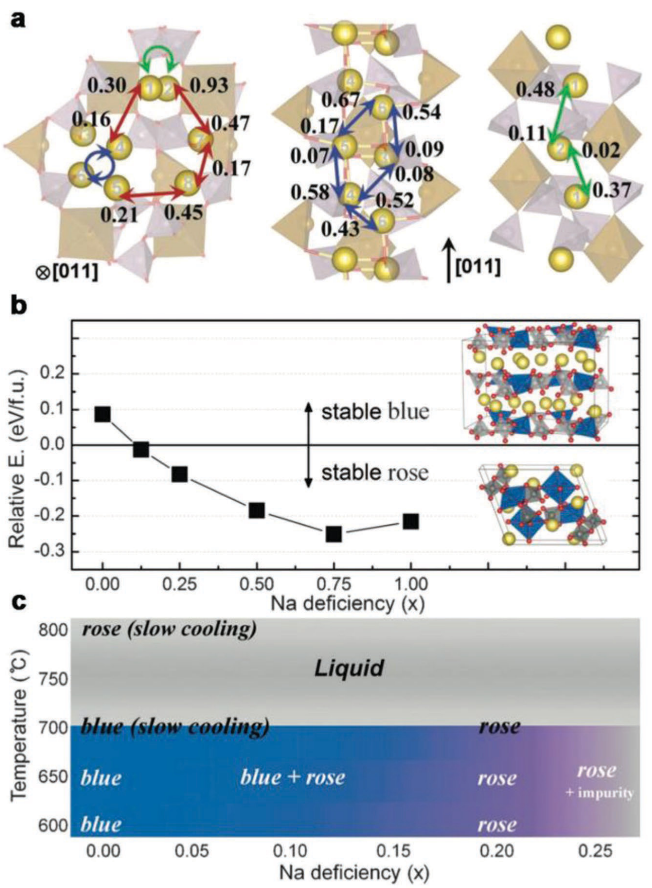

Figure 13. a) The calculated Na^+ migration pathways (arrows) and energy barriers (numbers in eV) in $Na_2FeP_2O_7$. Arrows in red indicate 2D migration paths, and those in green (Na1 and Na2 sites) and blue (Na3–Na6 sites) indicate the outward channels. Migration barriers along the [011] channel direction (green and blue) are shown in the two panels on the right. Reproduced with permission.[178] Copyright 2013, Wiley-VCH. b) Relative energies of the triclinic phase (rose) and conventional orthorhombic phase (blue) in $Na_{2-x}CoP_2O_7$ as a function of Na deficiency. Inset: Unit cell of the blue and rose phases. c) Synthesis map of $Na_{2-x}CoP_2O_7$ polymorphs as a function of Na deficiency. Reproduced with permission.[179] Copyright 2016, Wiley-VCH.

In addition, DFT studies[180] on $Na_4Mn_3(PO_4)_2(P_2O_7)$ proposed that the Jahn–Teller distortion of Mn^{3+} facilitates Na^+ diffusion in the crystal structure while maintaining the 3D diffusion framework. In contrast, the Na^+ migration barrier increases in $Na_4Fe_3(PO_4)_2(P_2O_7)$ due to the P_2O_7 distortion, leading to sluggish Na^+ diffusion kinetics.[181] A similar effect of polyanion distortion on Na^+ diffusion is also suggested in $Na_2MnP_2O_7$.[176]

Phase Transformation: Kim et al.[179] performed a joint computational and experimental study on the formation of the triclinic phase $Na_2CoP_2O_7$ instead of the conventional orthorhombic phase during synthesis. The triclinic phase polymorph of $Na_2CoP_2O_7$ achieved 40% higher energy density than the orthorhombic phase. DFT computation was performed to compare the energy of these polymorphs as a function of Na deficiency (Figure 13b). The calculations found that the formation of triclinic phase was energetically favorable at higher Na deficiency (Figure 13b), in agreement with the synthesis map identified in experiments (Figure 13c).[179] This study demonstrated the potential of using computation techniques in guiding the synthesis of new electrode materials for NIBs.

3.2.4. Sulfates

Besides phosphates, sulfates are also investigated as cathode materials for NIBs, as SO_4^{2-} is suggested to provide higher voltage than PO_4^{3-}.[182–184] Barpanda et al.[184] reported an alluaudite-type sulfate framework $Na_2Fe_2(SO_4)_3$ (**Figure 14**a) as a cathode material with a 3.8 V voltage and excellent rate capability. GGA+U calculations[184] of the $Na_2Fe_2(SO_4)_3$ structure identified Na2 sites as the most energetically favorable and Na3 sites as the least favorable (Figure 14b). The calculations found the Na^+ migration along 1D channels with low energy barriers (Figure 14b), in agreement with the fast charge–discharge kinetics observed in the experiments.[184] In addition, Na^+ migration has an energy barrier of 0.54 eV along Na2 channels and a low barrier of 0.28 eV along Na3 channels (Figure 14c).

3.2.5. Carbonophosphates

Another type of cathode with mixed polyanions is the carbonophosphates $Na_3MPO_4CO_3$ (M = Fe, Mn, Co, etc.),[25,26,32,185] which were first discovered as sodium cathodes through a high-throughput computation by Hautier et al.[32] While the high-throughput computational approach has been widely used in discovering new materials for a wide range of applications,[33,186,187] Hautier et al.[32] represents the first computation work in discovering new electrode materials for NIBs.[32] First principles computations by Hautier et al.[32] predicted that this structure is stable to host many TMs with desirable sodiation voltages of ≈3–4 V, which are within the safety window of the electrolytes. In particular, $Na_3MnPO_4CO_3$ has a high theoretical capacity of 191 mA h g^{-1} thanks to a two-electron redox between Mn^{2+} and Mn^{4+}.[26] The average redox potentials for Mn^{2+}/Mn^{3+} and Mn^{3+}/Mn^{4+} were calculated to be 3.1 and 4.0 V, respectively.[32] Chen et al.[26] successfully synthesized $Na_3MnPO_4CO_3$, and showed the voltage profile with two-electron redox reaction in good agreement with the computational predictions.[32] Huang et al.[185] performed DFT calculations to investigate the Na^+ diffusion in $Na_3FePO_4CO_3$, and identified the energy barriers of the pathway along b and c axis to be 0.6 and 0.7 eV, respectively, in agreement with the limited rate capability of $Na_3FePO_4CO_3$ from the experiments.

3.2.6. NASICON

The NASICON structure, which is originally investigated as fast Na-ion conductors, is also developed as a cathode material for NIBs. The composition $Na_xV_2(PO_4)_3$ (**Figure 15**a) is demonstrated with good electrochemical performance with respect to capacity, cyclability, rate capability, and stability.[20,188,191–193] The voltage profile of $Na_xV_2(PO_4)_3$, from first principles computation, is in good agreement with experiments.[189,190,194] A voltage plateau of 3.40 V is identified for desodiation from

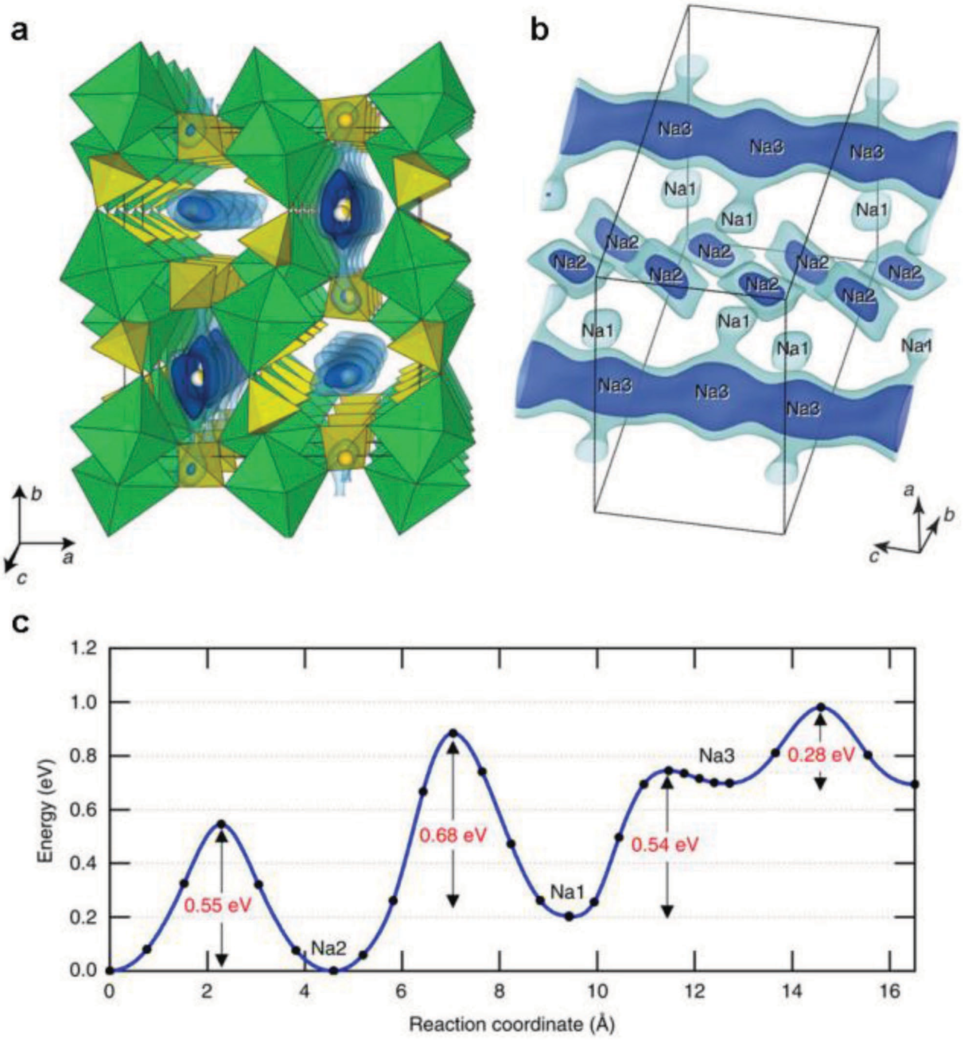

Figure 14. Na^+ diffusion in $Na_2Fe_2(SO_4)_3$. a,b) Isosurfaces of the difference of the bond valence sum (ΔBVS). The blue and light-blue surfaces are for $\Delta BVS = 0.2$ and 0.4, respectively. Inner side of the surface corresponds to accessible spaces for Na^+. Green and yellow polyhedra are FeO_6 and SO_4, respectively. c) Na^+ migration energy from NEB calculations. Reproduced with permission.[184] Copyright 2014, Nature Publishing Group.

$x = 3$ to $x = 1$ (Figure 15b), corresponding to a two-phase transition from $Na_3V_2(PO_4)_3$ to $NaV_2(PO_4)_3$.[188] During the desodiation, Na^+ was found to be first removed from Na2 sites as shown by the Na site occupancy from the computation (Figure 15a).[189] In addition, first principles computation also indicated a high voltage plateau of 4.64 V ($0 \le x \le 1$) and a low voltage plateau of 2.03 V ($3 \le x \le 4$).[189] An extra low plateau of 0.3 V by inserting Na^+ from $x = 4$ to 5 is also shown in the computation and is demonstrated in the experiments.[194] First principles computation confirmed low migration barriers of Na^+ diffusion in the open channels of NASICON structural framework,[190] confirming its good reversibility and decent rate capabilities during electrochemical cycling (Figure 15c). Ong et al.[12] studied the phase transformation of Li and Na NASICON structures, and found that $Na_3V_2(PO_4)_3$ energetically prefers the rhombohedral $R\bar{3}c$ structure and $Li_3V_2(PO_4)_3$ prefers the monoclinic $P1121/n$ structure, in agreement with experimental observations.[195,196]

3.3. Organic Compounds

Organic materials, e.g., disodium rhodizonate ($Na_2C_6O_6$)[197,198] and benzoquinone derivatives,[199] have been demonstrated as NIB cathode materials with good electrochemical performance, low cost, and environmental friendliness, thanks to the absence of transition metal elements.[200–202] The computational techniques for inorganic materials are also applied to study the organic compounds in NIBs. However, a significant technical difficulty is that the atomistic structures of the sodiated organic compounds are often unknown. In order to perform the calculations on these organic solids, their atomistic structures need to be computationally generated from structure prediction algorithms, e.g., the USPEX algorithm.[203–205]

Yamashita et al.[66] studied the structures and packing of sodiated $Na_xC_6O_6$ using the USPEX structure prediction algorithm, and reproduced the calculation voltage in agreement with the experiments.[198] Kim et al.[199] studied $C_6R_4O_2$ (R = F,

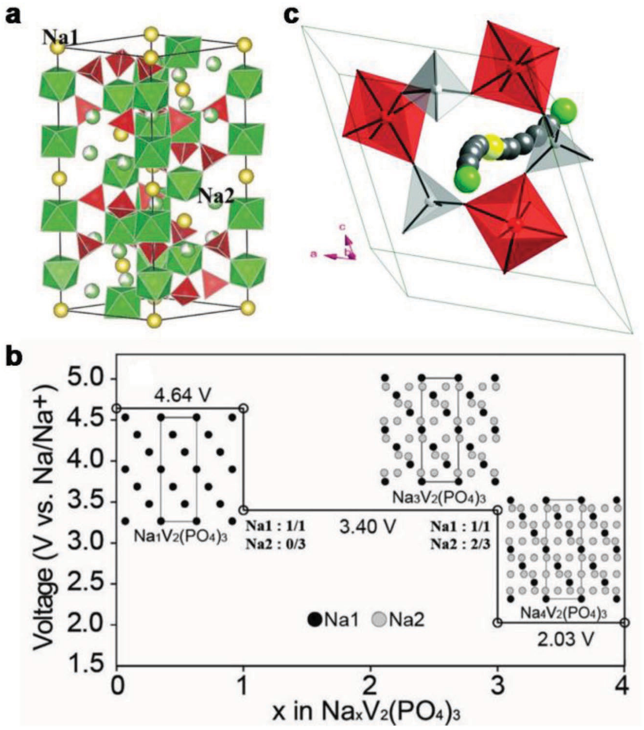

Figure 15. a) Crystal structure of $Na_3V_2(PO_4)_3$. Reproduced with permission.[188] Copyright 2017, Wiley-VCH. b) Calculated voltage profile of $Na_xV_2(PO_4)_3$ ($0 \leq x \leq 4$). Reproduced with permission.[189] Copyright 2012, The Electrochemical Society. c) Na^+ diffusion pathway through the hexagonal bottleneck in NASICON structure. Reproduced with permission.[190] Copyright 2015, Royal Society of Chemistry.

Cl, Br) to increase the redox potential and energy density, and found that the substitution of O with halogen atoms indeed decreased the lowest unoccupied molecular orbital (LUMO) and increased the redox potential. In particular, $C_6Cl_4O_2$ was demonstrated in their experiments with good electrochemical performances. Araujo et al.[67] studied the crystal structures of $Na_xC_6Cl_4O_2$ using the USPEX structure prediction algorithm and reproduced the experimental voltage profile. They also found that hybrid functional calculations provided more accurate energies for these organic compounds. In an integrated computational and experimental study, Wu et al.[202] studied and demonstrated the $Na_2C_6H_2O_4$ for Na insertion at a much lower voltage. The DFT computation confirmed the voltage and reaction mechanism observed in experiments, and confirmed the charge compensation mechanism during sodiation. These studies demonstrated the computational capability in studying organic electrode materials. Recently, computational studies were extended to novel compounds, such as polyaniline (PANI),[206] tetracyanoethylene (TCNE),[207] etc., as potential electrodes for NIBs.

4. Negative Electrode Materials

A major challenge in NIBs is the lack of good anode materials. Graphite anodes commercially used in LIBs cannot be used in NIBs, as Na does not intercalate into graphite.[5,208–211] This challenge motivates the exploration of a broader range of anode materials for NIBs, including carbonaceous anodes (Section 4.1), alloying anodes (Section 4.2), conversion reaction anodes (Section 4.3), sodium titanium oxides (Section 4.4), and other materials (Section 4.5).

4.1. Carbonaceous Anode

While graphite is a widely used anode material for lithium ion batteries (LIBs),[214–216] many experimental studies reported poor Na insertion and low Na capacity (<35 mA h g^{-1}) in graphite, which cannot be used as an anode for NIBs.[208–211] While some mistakenly attributed poor Na intercalation to large Na ion size, other alkali ions such as K, Rb, Cs with even larger ionic radii show reversible intercalation in graphite with decent capacity.[217] Multiple computation studies[212,218] using GGA and vdW functionals confirmed that the formation of NaC_6 or NaC_8 was energetically unfavorable with positive formation energies, in contrast to the favorable formation of AC_x (A = Li, K), indicating the origin of poor Na insertion in graphite is thermodynamically intrinsic.

To further understand why Na insertion has positive formation energies in graphite, Liu et al.[212] decomposed the alkali intercalation process in AC_x (A = Li, Na, K, Rb, Cs) into three physical components, i.e., binding, graphite straining, and metal decohesion (**Figure 16**a), and quantified the energy contribution of each component. By analyzing the trend of energy contributions from each physical component (Figure 16a), they attributed the weak binding between Na and graphite as the limiting factor for the unfavorable Na intercalation in graphite.

Poor Na storage in graphite motivates the discovery of other carbonaceous anodes, such as hard carbon and soft carbon with higher capacities.[211,219–221] Many disordered carbons used for NIB anodes have a larger interlayer distance and more defects than those of graphite.[211,222] First principles computation studied the effects of the carbon interlayer distances and defects on Na intercalation. Cao el al.[213] calculated the reaction energies of Li and Na ions intercalation between carbon layers as a function of interlayer distance (Figure 16b). These calculations revealed that Na^+ insertion has higher energy cost than Li^+ insertion between carbon layers and that Na^+ insertion is energetically unfavorable at the carbon interlayer distance of graphite. The calculations also found that the energy of Li^+/Na^+ insertion decreases (i.e., becomes more favorable) as the interlayer distance increases. Tsai et al.[63] confirmed the same trend of Na^+ insertion energies on carbon interlayer distances using various vdW corrections. In addition, Tsai et al.[63] investigated the effects of various point defects, such as mono-vacancy, divacancy, and Stone-Wales defects, on Na^+ insertion, and found that all these defects make Na^+ insertion more energetically favorable due to the binding between Na^+ and defects. Therefore, the increased carbon interlayer distance and defects in these disordered carbon materials, such as hard carbon and soft carbon, can significantly enhance Na^+ insertion. Tsai et al.[63] also found that the sloping voltage region of charge–discharge curves of disordered carbon observed in experiments[222] corresponds to Na adsorption on defective carbon surfaces and that the flat voltage region corresponds to Na intercalation into the

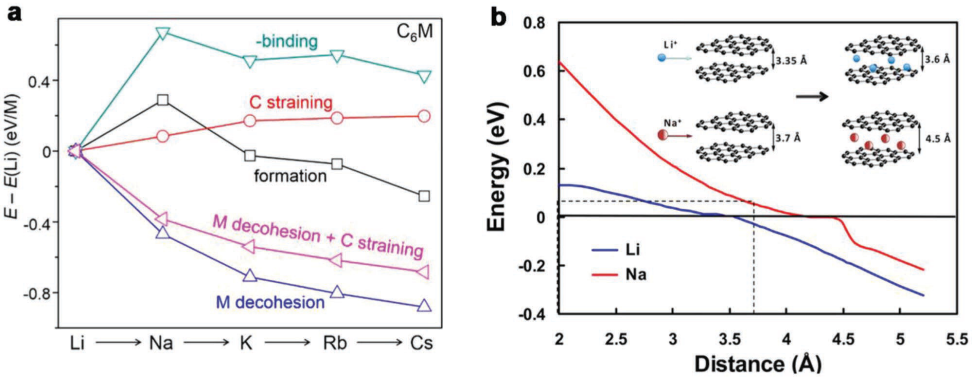

Figure 16. a) Energy contributions from binding (green), graphite straining (red), and metal decohesion (blue) to the formation of AC$_6$ (A = Li, Na, K, Rb, Cs). Reproduced with permission.[212] Copyright 2016, United States National Academy of Sciences. b) Calculated reaction energies for Na (red) and Li (blue) insertion into carbon layers as a function of the interlayer distance. Reproduced with permission.[213] Copyright 2012, American Chemical Society.

carbon layers. These computational studies provide the theoretical basis for the significantly improved Na storage in the disordered carbon materials.

4.2. Alloying Anode

As potential NIB anodes, alloying compounds have high theoretical capacities and low Na insertion potentials.[20,223,224] Na-binary alloys with Group 14 elements, such as Si, Ge, Sn, Pb, and Group 15 elements, such as P, As, Sb, Bi, have demonstrated high Na capacities of 370–2600 mA h g^{-1}.[20,225,226]

Low voltage and high capacity are desired properties for anode materials. Chevrier et al.[22] calculated the voltage profiles of Na alloying reactions in Group 14 elements Si, Ge, Sn, Pb (**Figure 17**a). These Group 14 alloys show low Na insertion voltages of <0.8 V suitable for anode applications. The sodiation voltage profiles of Group 15 elements P, As, Sb, Bi evaluated by Mortazavi et al.[226] (Figure 17b) also show low voltages ranging from 0.4 to 1.2 V, suggesting Group 15 alloys as potential anode materials. The calculated voltage profiles for the sodiation of P, Sb, Pb, Bi are in good agreement with experimental results.[44,227–229]

4.2.1. Group 14 Elements

While Si and Ge show high capacities for lithiation, the sodiation capacities of Si and Ge are much lower than those of Sn and Pb.[20] Chou et al.[230] evaluated the structural evolution and energies of sodiated crystalline and amorphous phases of Si, Ge, Sn (**Figure 18**), and found that c-Na$_x$Sn alloy has the lowest formation energies. The formation energies continuously decrease upon sodiation until $x = 3.75$, indicating energetically favorable sodiation for up to 3.75 Na per Sn. Their computational results of c-Na$_x$Sn agree with the experimental facts that high specific capacity of Na-Sn alloys can be achieved in Na$_{15}$Sn$_4$ (i.e., Na$_{3.75}$Sn).[231] In contrast, the formation energies of c-Na$_x$Ge and c-Na$_x$Si only decrease from 0 to 1 upon sodiation, but exhibit a positive trend at $x > 1$ (Figure 18). Therefore, the high formation energies of the alloy compounds at $x > 1$ (e.g., c-Na$_{3.75}$Si and c-Na$_{3.75}$Ge) confirm the thermodynamic origin of limited sodiation capacity in Si and Ge, in agreement with the bulk phase calculations[22,230,232] and experiments[233,234] that only one Na can be inserted per Ge and Si forming NaGe and NaSi.

The computation studies by Chou et al.[230] also found amorphous alloys, which are widely observed during sodiation experiments,[235–237] have favorable energies and faster kinetics of Na$^+$ diffusion. The formation of amorphous alloy phases a-Na$_x$Si and a-Na$_x$Ge was found to have lower formation energies (Figure 18) compared to crystalline phases.[230,232] In addition, AIMD simulations[230] observed facile Na$^+$ diffusion in amorphous NaM phases (M = Si, Ge, Sn) with low activation energies of 0.26–0.31 eV and high Na$^+$ diffusivities of 8×10^{-9} to 3×10^{-8} cm^2 s^{-1} at 298 K. Facile Na$^+$ diffusion in a-Na$_{0.75}$Si with an activation energy of 0.38 eV was also reported by Jung et al.[232] In contrast, NEB calculations reported high activation energies of 1.08–1.15, 0.78, and 0.53 eV, for single-Na$^+$ hops in c-M, where M = Si, Ge, Sn, respectively, at the dilute limit.[230,232,238] These computational studies suggest faster Na$^+$ diffusion kinetics in amorphous alloys and confirm the kinetically favored formation of amorphous alloys observed during sodiation.[235–237]

4.2.2. Group 15 Elements

Among Group 15 elements, phosphorous exhibits the highest theoretical capacity of 2596 mA h g^{-1}[5,223] and has drawn great attention as a highly promising anode material.[239–244] Computational studies were performed for the structural evolution, structure, and Na$^+$ diffusion in black phosphorous. In addition to the voltage profile calculated from known Na–P compounds (Figure 17b),[226] a number of computational studies are performed to explore intermediate phases that may form during Na insertion. Using a random structure search method, Mayo et al.[245] predicted a number of new compounds, such as Na$_3$P$_7$ and Na$_5$P$_4$, as intermediate phases during sodiation. They also observed that, as Na ions were inserted into the black phosphorous structure, P layers were gradually broken into cages, semi-layers, broken chains, and eventually to isolated P ions in Na$_3$P. The computation by Hembram et al.[246] suggests the sodiation starts with Na intercalation up to Na$_{0.25}$P, and the following

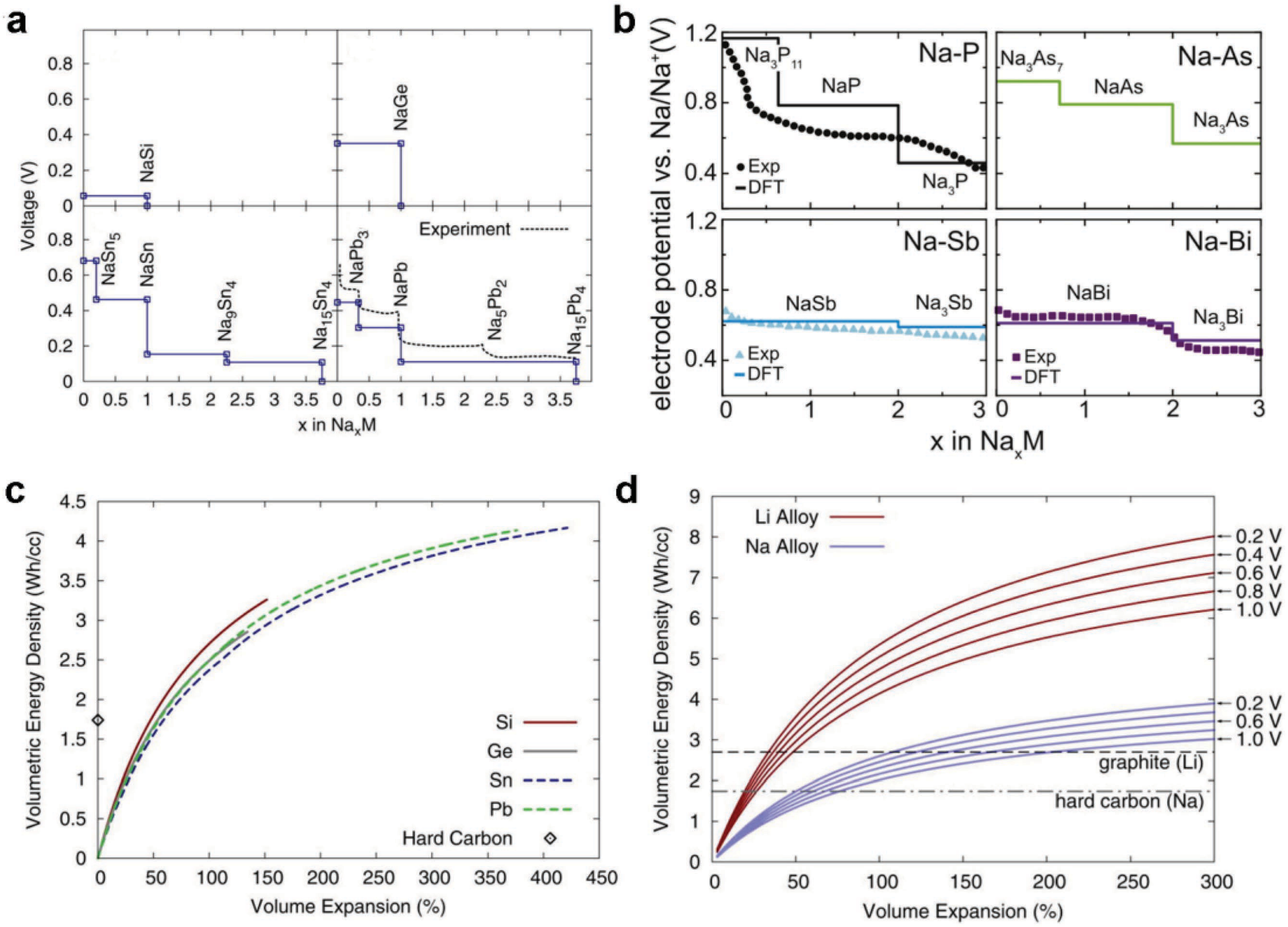

Figure 17. a) Calculated equilibrium voltage profiles of Na_xM with Group 14 elements M = Si, Ge, Sn, Pb. Reproduced with permission.[22] Copyright 2011, The Electrochemical Society. b) Calculated equilibrium voltage profiles of Na_xM with Group 15 elements M = P, As, Sb, Bi. Reproduced with permission.[226] Copyright 2015, Elsevier. c) Volumetric energy density of Na_xM (M = Si, Ge, Sn, Pb) as a function of volume expansion. d) Universal volume expansion curves for Li and Na alloys at different assumed anode potentials and at a hypothetical cathode potential of 3.75 V. Reproduced with permission.[22] Copyright 2011, The Electrochemical Society.

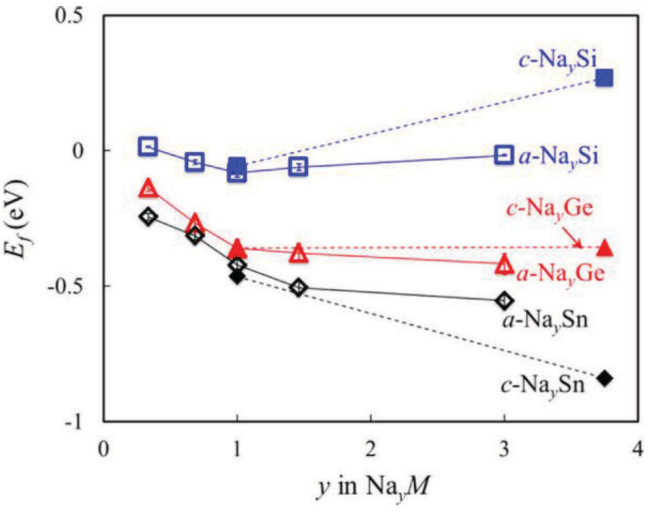

Figure 18. Formation energies of Na_xM (M = Si, Ge, Sn) in crystalline phases c-Na_xM and amorphous phases a-Na_xM. Reproduced with permission.[230] Copyright 2015, American Chemical Society.

sodiation is accompanied by the breaking of P-P bonds and the structure amorphization. The Na^+ diffusion mechanism is also investigated in multiple computational studies.[246–249] Various computational studies[246,247,249] found that Na^+ diffusion in black phosphorous at the dilute limit of Na is highly anisotropic, where Na^+ diffusion has a low migration barrier of 0.18–0.76 eV within P planes and a higher barrier of 4.2 eV between P planes.

4.2.3. Volumetric Energy Density

While some alloying elements show high capacity, the large size of Na limits the volumetric energy density of these anodes.[22] Based on the DFT calculations, Chevrier et al.[22] quantified the volume expansion as a function of sodiation levels (Figure 17c) from the calculated voltage curves, and estimated the volumetric energy densities of Na_xM (M = Si, Ge, Sn, Pb) alloys based on an assumed cathode potential of 3.75 V. The NIB cells using Na_xSn or Na_xPb anode with an insertion of 3.75 Na lead to higher volumetric energy densities compared to hard carbon anodes.[22,250] In addition, Na_xM alloys with Group 15 M (M = P, As, Sn, Bi) also exhibit high volumetric densities if fully sodiated.[226] Chevrier et al.[22] revealed that a single Na occupies a constant volume of 30.3 Å^3 in Na_xM alloys, independent of M and the sodiation level x. The volume occupied by a single Na in these alloys is therefore about twice as large as that of Li (14.8 Å^3).[22,251] As a result of the larger volume of Na in these alloys, the volumetric energy densities in Na-based alloys are much lower than those of Li-based alloys (Figure 17d). The volumetric energy densities of Na-based alloys are only about half of those of Li-based alloys at the same volume expansion (Figure 17d). Na-based alloys with 300% volume expansion can only achieve the volumetric energy densities that Li-based alloys can achieve with only 50–100% volume expansion, making Na alloying anodes significantly underperform their Li counterparts. Therefore, low volumetric energy density of Na alloying anodes is a significant disadvantage compared to their Li counterparts.[22]

The substantial volume expansion and contraction during electrochemical cycling cause mechanical failures and electrochemical capacity losses.[226,252] This problem is more severe in Na alloying anodes than in Li counterparts.[20,22,226,252] For example, the calculations found Na_xSn has the highest volume expansion of ≈425% at $Na_{3.75}Sn$, in agreement with experimental values.[231,253] It is a significant challenge to deal with the large volume expansion of Na alloying anodes. In addition, DFT calculations[230,252] also found bulk moduli of Na_xM (M = Si, Ge, Sn, P, As, Sb, Bi) decrease during sodiation ($0 \le x \le 1$). Therefore, understanding the mechanical failure during volume expansion and establishing an effective mitigation strategy for the volume expansion are needed to enable high-performance Na alloying anodes.

4.3. Conversion Reaction Anode

In addition to alloying anodes, conversion reaction anodes M_aX_b, where M is metal (e.g., Sn, Sb, Fe, Mo, Co and Ni) and X is O, S, and Se, etc., have been explored as high-capacity anode materials for NIBs.[255–259] The reaction pathways of these materials are complicated. Commonly, their sodiation reaction starts with a small amount of Na intercalation to form $Na_xM_aX_b$, followed by the conversion reaction to form Na_2X and metallic M, and some of the metals, such as Sn and Sb, may further react through Na alloying.[255–259] Klein et al.[254] used the same computation scheme in Section 2.1 and experimental thermodynamic data to evaluate and compare the lithiation and sodiation potentials for materials M_aX_b with a variety of cations and anions (**Figure 19**a). The sodiation conversion reactions in general lead to lower potentials than those of lithiation conversion reactions. In particular, replacing lithium by sodium in conversion reactions of oxides leads to lower potentials by ≈1 V. Klein et al.[254] illustrated the trend of conversion potentials, and showed that conversion reactions in halides often exhibit higher potentials than those in chalcogenides. Phosphides and hydrides exhibit even lower potentials. Among chalcogenides,

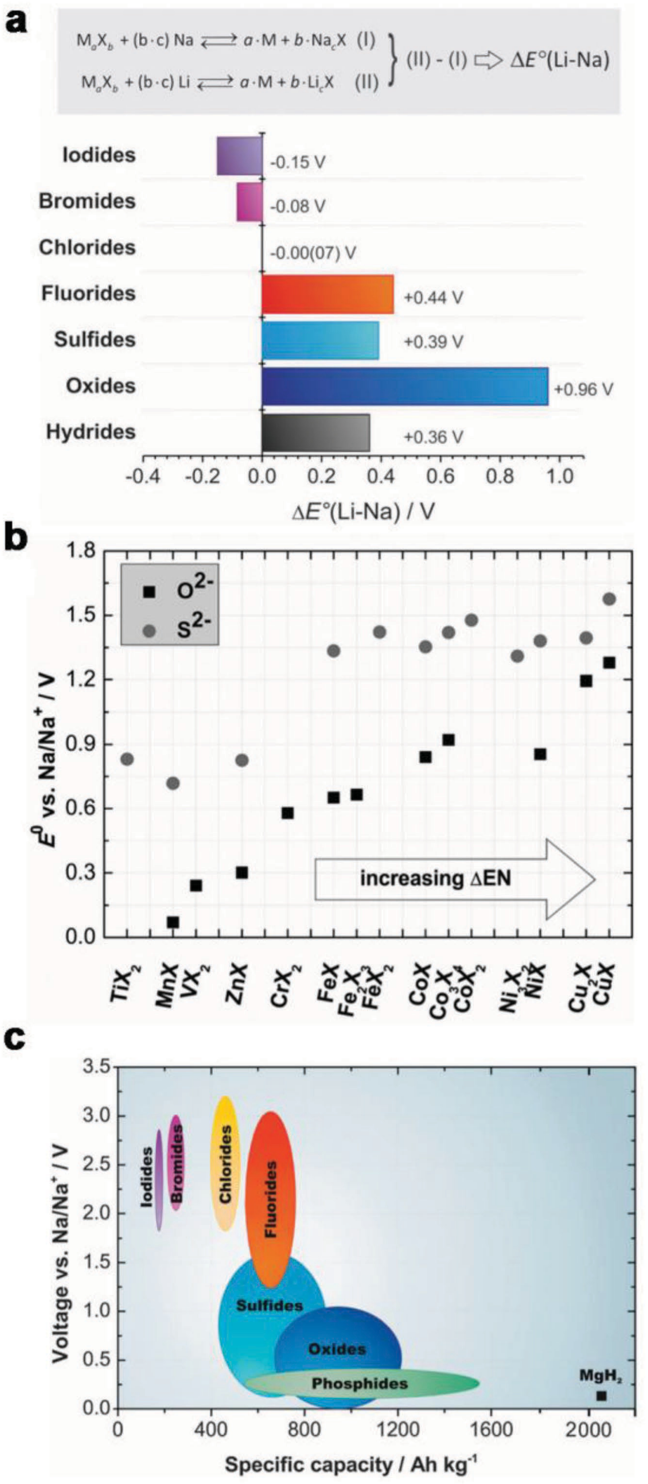

Figure 19. a) Calculated voltage differences between conversion reactions of M_aX_b under sodiation and lithiation. Positive values correspond to higher voltages for the lithiation conversion reactions. b) Calculated standard potentials for different transition metal chalcogenides. c) Specific capacities and potentials for sodiation conversion reactions in different materials classes. Reproduced with permission.[254] Copyright 2013, Royal Society of Chemistry.

sulfides have higher potentials than those of oxides with the same cations M (Figure 19b). For investigated M_aX_b materials, oxides and sulfides have sodiation potentials of 0.1–1.3 and 0.7–1.6 V, respectively, which can be considered as anode materials in NIBs. Figure 19c shows an overview of the calculated equilibrium potentials and theoretical capacities of sodium conversion reactions. These calculations over a range of chemistry provide a valuable guidance for future selection of conversion reaction electrodes for NIBs.

Similar to alloying reactions, conversion reactions also have the problem of large volume changes during cycling and low columbic efficiency caused by irreversible reactions.[223,254] Klein et al.[254] evaluated the volume expansion of conversion reactions, and found that a large volume expansion of 130–430% in phosphides, 75–300% in oxides and sulfides, and 35–90% in halides.

In addition, the atomistic mechanisms of Na conversion reactions were studied by first principles computation.[260–262] Yao et al.[261] studied the conversion reaction of Sb_2S_3 anode for phase transformation, Na-ion diffusion, and electronic structure. Their computation identified the reaction pathways of Na conversion reaction using thermodynamic phase equilibria, and found Sb_2S_3 first undergoes a Na intercalation process to form $Na_xSb_2S_3$, then undergoes conversion and alloying reactions to form Na_3Sb and Na_2S. The calculations identified low Na^+ migration barriers in these intermediate phases. In addition, the computation found significantly increased electronic conductivity upon the formation of $Na_xSb_2S_3$ during sodiation, and the observed good electrochemical performance was attributed to the facile Na^+ diffusion and good electronic conductivity in the intermediate conversion reaction products.[261]

Given the complexity of reaction pathways and amorphous structures, AIMD simulations were employed to study reaction mechanisms in conversion reactions.[261,262] Using AIMD simulations, He et al.[262] observed a significant higher rate of lithiation in NiO than that of sodiation. In addition, AIMD simulations also observed the formation of a passivation layer of Na_2O during the sodiation, while the lithiation continued into the entire structure, consistent with in situ TEM observations.[262] In addition to studying diffusion mechanisms, AIMD simulations may play an important role in revealing the reaction mechanisms of complex systems such as alloying, conversion, and interphase reactions.

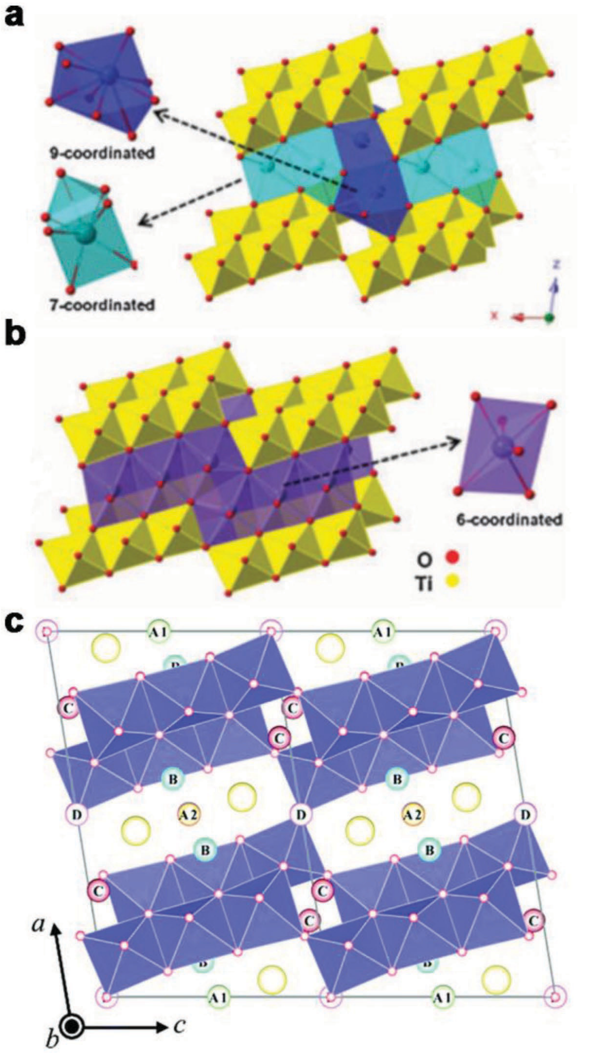

Figure 20. Crystal structures of a) $Na_2Ti_3O_7$ and b) $Na_4Ti_3O_7$. TiO_6 octahedra (yellow) and Na-O polyhedra with different coordination numbers are shown. Reproduced with permission.[270] Copyright 2014, Royal Society of Chemistry. c) Crystal structure and possible Na interstitial sites in $Na_2Ti_6O_{13}$. Reproduced with permission.[271] Copyright 2017, Royal Society of Chemistry.

4.4. Sodium Titanium Oxides

Given the good cycling performance of lithium titanate materials for LIBs, titanium oxide compounds are investigated as potential anode materials for NIBs.[263–269] We review computation studies of $Na_{2+x}Ti_3O_7$ (Section 4.4.1), $Na_{2+x}Ti_6O_{13}$ (Section 4.4.2), and spinel titanate materials (Section 4.4.3).

4.4.1. $Na_{2+x}Ti_3O_7$

$Na_{2+x}Ti_3O_7$ ($0 \leq x \leq 2$), as a promising anode material for NIBs, is demonstrated to have low Na^+ intercalation potential (≈0.3 V) and high specific capacity (≈180 mA h g^{-1}).[263,270] The structure of $Na_2Ti_3O_7$ forms a 2D layered framework of edge-sharing TiO_6 octahedra. Na ions are located at two types of sites, which are coordinated by nine and seven oxygen ions, respectively (**Figure 20**a). Senguttuvan et al.[263] reported that $Na_2Ti_3O_7$ can reversibly intercalate two Na ions per formula unit during electrochemical cycling, forming the fully sodiated phase $Na_4Ti_3O_7$. DFT calculations[270,272] studied the structures of fully intercalated $A_4Ti_3O_7$ (A = Na or Li) and found that the A^+ insertion results in the rearrangement of alkali ions and the change of the Ti–O framework (Figure 20b). All alkali ions were coordinated by six oxygen ions in $A_4Ti_3O_7$ instead of nine or seven oxygen ions in $A_2Ti_3O_7$. This structural rearrangement of $A_4Ti_3O_7$ after sodiation agrees with experimental characterizations.[263,270] The calculated intercalation voltages[270] from $A_2Ti_3O_7$ to $A_4Ti_3O_7$ are 0.4 and 1.7 V for sodiation and lithiation, respectively, which agree with experimental values of

0.3 and 1.6 V.[272] Pan et al.[273] investigated Na^+ diffusion mechanism in $Na_2Ti_3O_7$ using NEB methods and identified vacancy hopping mechanism forming zigzag diffusion pathways. Na^+ migration has an energy barrier as low as 0.18–0.23 eV between TiO_6 octahedron layers.

4.4.2. $Na_{2+x}Ti_6O_{13}$

$Na_{2+x}Ti_6O_{13}$ shows high-rate performance and good cycle life.[264] $Na_2Ti_6O_{13}$ has the open crystal structure framework with 3D tunnels along the *b* direction formed by linking TiO_6 octahedra (Figure 20c). Host Na ions in $Na_2Ti_6O_{13}$ are accommodated inside the tunnels (yellow sites in Figure 20c), and additional Na ions are inserted into the interstitial sites upon sodiation. Ling et al.[271] studied the preferred sites for Na insertion among all possible interstitial sites using GGA+U calculations, and found that the first Na ion inserted into A1 sites and the second Na ion into B sites (Figure 20c). On the basis of computationally determined structures of sodiated phases, the Na insertion voltage from $Na_2Ti_6O_{13}$ to $Na_3Ti_6O_{13}$ was calculated to be 0.75 V, in agreement with the experimental values (≈0.8 V).[264] However, further sodiation from $Na_3Ti_6O_{13}$ to $Na_4Ti_6O_{13}$ was calculated to be energetically unfavorable. Previous GGA calculations by Shen et al.[274] predicted a similar first voltage plateau of 0.73 V, but a favorable Na intercalation from $Na_3Ti_6O_{13}$ to $Na_4Ti_6O_{13}$ with a 0.15 V potential. The discrepancy between these two computation studies may be caused by the energy difference between GGA and GGA+U methods. In addition, Ling et al.[271] calculated Na^+ migration energies along various diffusion pathways using NEB calculations. The facile Na^+ diffusion occurs with low migration energies of 0.24 and 0.41 eV between A1 sites for vacancy and dilute single Na ion, respectively. These calculation results of low Na^+ migration barriers support the high cycling rate of $Na_{2+x}Ti_6O_{13}$ observed in experiments.[264]

4.4.3. Spinel Titanate

$Li_4Ti_5O_{12}$ is known as a long-cycle-life anode for LIBs.[275] Sun et al.[269] reported the spinel compound as a NIB anode with an average voltage of 0.91 V and excellent cyclability. To understand the sodium insertion mechanism in $Li_4Ti_5O_{12}$, DFT calculations combined with experimental analyses were performed.[269] The calculations predicted a three-phase separation mechanism for sodium storage in $Li_4Ti_5O_{12}$, in agreement with in situ synchrotron XRD.[269] In addition, Na^+ migration barriers were calculated using NEB methods, confirming the reversible Na insertion into the octahedral sites of the spinel host.

4.5. Other Materials

In addition to graphite, many other layered materials are also studied for NIB anodes. Liu et al.[212] computationally demonstrated weak binding between Na and other 2D layered materials, such as MoS_2, TiS_2, and V_2O_5, and found the weak binding between Na and host materials. As a general phenomenon, this weak binding between Na and other materials has implications for many battery-related materials properties.[12,212] The weak binding of Na would result in small energy cost during sodiation and yield small intercalation voltage (with respect to Na/Na^+), which is desired for the anode but not for the cathode.[12] A first principles computational study by Ong et al.[12] demonstrated that the sodiation potential are in general lower than the lithiation potential in a wide range of materials. Therefore, the electrode materials that are ideal in LIBs may not be the best choice for NIBs. In addition, the weaker Na binding would lead to lower Na^+ migration barriers in materials and faster Na^+ diffusion kinetics. Facile Na^+ diffusion in many materials are confirmed by computational and experimental studies.[12,23,230] Indeed, high rate performance during electrochemical cycling has been widely reported in many NIB electrode materials.[20,223] Therefore, NIBs may be promising for high-power and high-rate energy storage applications.

Recently, some computational studies investigated the possibility of 2D layered materials as anode materials for NIBs.[21,64,65,246,276–282] 2D layered materials can either accommodate Na ions between 2D layers or absorb Na ions on surfaces. Ling et al.[276] studied electrochemical properties of boron-doped graphene using first principles computation, and predicted boron-doped graphene as an anode material with high specific capacity, low insertion voltage, and fast Na^+ kinetics. Other layered materials, e.g., transition metal dichalcogenides,[21,277,282] phosphorene,[64,246] metal carbides,[278] and borophene,[281] have also been proposed as potential anode materials for NIBs by computational investigations. However, many 2D materials worsen the problems of low volumetric density of Na anode and may exhibit significant surface decomposition against the electrolyte during electrochemical cycling.[239,283] The application of 2D materials for NIBs is yet to be demonstrated.

5. Perspective and Concluding Remarks

While sodium-based chemistry for electrochemical energy storage, such as sodium–sulfur and Zebra cells, has been long developed, the recent renaissance of NIBs is largely motivated by strong demand for low-cost and large-scale energy storage applications such as for the electric grid.[1] The extensive knowledge obtained from LIBs in the last three decades have set the research and development of NIBs on a fast track, and current state-of-the-art NIBs have achieved reasonably high energy density and long cycle life.[5–7,20]

While significant understanding of the electrode materials in NIBs has been achieved through computational and experimental studies, as shown in this review, the investigations of various battery materials, such as cathodes, anodes, electrolytes, and current collectors, are still needed to further improve their properties and to push the performance of NIBs to match or exceed current LIBs. For example, rational design strategies of electrode materials to fine tune the phase transformations and cation orderings at different sodiation levels are yet to be developed for improving the reversibility of electrochemical cycling in NIBs. As demonstrated in various studies reviewed here, the computational and modeling techniques provide unique fundamental understanding of the materials, such as the energies of various intermediate phases and atomistic-scale diffusion mechanisms, which are often difficult to directly characterize in experiments. The complementary integration of computations and experiments has successfully accelerated the research in multiple fields. The utilization of advanced computational techniques with experimental characterizations may provide further opportunities in the field to enhance understanding of materials and to design novel materials with high performance.

Furthermore, the predictive power of computation enhances the capability to design new electrode and electrolyte materials. Currently, the design and development of NIB electrode materials mainly focuses on the optimization and modification of known electrode materials and structures. Given that there are significantly more sodium compounds than lithium compounds, using a computational approach to discover novel electrode materials will be extremely valuable in satisfying ever-increasing demand for high energy density and fast charging rate. Computation accelerated design and discovery based on the Materials Genome type approach[284] for completely novel NIB electrode materials are of great potential. The recent emergency of artificial intelligence and machine learning techniques may significantly aid the materials search, discovery, and screening.[285–287] These practices are expected to bring further breakthroughs to next-generation high-performance NIBs.

Acknowledgements

Q.B. and Y.M. acknowledge the financial support by Office of Naval Research and by U.S. Department of Energy, Office of Energy Efficiency and Renewable Energy. H.C. and L.Y. acknowledge the finical support by the U.S. National Science Foundation under grant numbers DMR-1410936 and CBET-1706723. L.Y. acknowledges the scholarship from the China Scholarship Council.

Conflict of Interest

The authors declare no conflict of interest.

Keywords

anodes, cathodes, first principles calculations, sodium ion batteries, sodium-ion intercalation

Received: October 27, 2017
Revised: December 29, 2017

---

[1] B. Dunn, H. Kamath, J. M. Tarascon, *Science* **2011**, *334*, 928.
[2] H. Pan, Y.-S. Hu, L. Chen, *Energy Environ. Sci.* **2013**, *6*, 2338.
[3] M. R. Palacin, *Chem. Soc. Rev.* **2009**, *38*, 2565.
[4] S. W. Kim, D. H. Seo, X. Ma, G. Ceder, K. Kang, *Adv. Energy Mater.* **2012**, *2*, 710.
[5] N. Yabuuchi, K. Kubota, M. Dahbi, S. Komaba, *Chem. Rev.* **2014**, *114*, 11636.
[6] H. Yoshida, N. Yabuuchi, K. Kubota, I. Ikeuchi, A. Garsuch, M. Schulz-Dobrick, S. Komaba, *Chem. Commun.* **2014**, *50*, 3677.
[7] N. Yabuuchi, M. Kajiyama, J. Iwatate, H. Nishikawa, S. Hitomi, R. Okuyama, R. Usui, Y. Yamada, S. Komaba, *Nat. Mater.* **2012**, *11*, 512.
[8] R. J. Clément, P. G. Bruce, C. P. Grey, *J. Electrochem. Soc.* **2015**, *162*, A2589.
[9] E. de la Llave, E. Talaie, E. Levi, P. K. Nayak, M. Dixit, P. T. Rao, P. Hartmann, F. Chesneau, D. T. Major, M. Greenstein, *Chem. Mater.* **2016**, *28*, 9064.
[10] L. Liu, X. Li, S. H. Bo, Y. Wang, H. Chen, N. Twu, D. Wu, G. Ceder, *Adv. Energy Mater.* **2015**, *5*, 1500944.
[11] Y. Wang, R. Xiao, Y.-S. Hu, M. Avdeev, L. Chen, *Nat. Commun.* **2015**, *6*, 6954.
[12] S. P. Ong, V. L. Chevrier, G. Hautier, A. Jain, C. Moore, S. Kim, X. Ma, G. Ceder, *Energy Environ. Sci.* **2011**, *4*, 3680.
[13] S. Komaba, C. Takei, T. Nakayama, A. Ogata, N. Yabuuchi, *Electrochem. Commun.* **2010**, *12*, 355.
[14] S. Kikkawa, S. Miyazaki, M. Koizumi, *J. Power Sources* **1985**, *14*, 231.
[15] Y. Takeda, K. Nakahara, M. Nishijima, N. Imanishi, O. Yamamoto, M. Takano, R. Kanno, *Mater. Res. Bull.* **1994**, *29*, 659.
[16] C. Delmas, J. J. Braconnier, C. Fouassier, P. Hagenmuller, *Solid State Ionics* **1981**, *3*, 165.
[17] A. Mendiboure, C. Delmas, P. Hagenmuller, *J. Solid State Chem.* **1985**, *57*, 323.
[18] J. J. Braconnier, C. Delmas, P. Hagenmuller, *Mater. Res. Bull.* **1982**, *17*, 993.
[19] A. Maazaz, C. Delmas, P. Hagenmuller, *J. Inclusion Phenom.* **1983**, *1*, 45.
[20] H. Kim, H. Kim, Z. Ding, M. H. Lee, K. Lim, G. Yoon, K. Kang, *Adv. Energy Mater.* **2016**, *6*, 1600943.
[21] E. Yang, H. Ji, Y. Jung, *J. Phys. Chem. C* **2015**, *119*, 26374.
[22] V. L. Chevrier, G. Ceder, *J. Electrochem. Soc.* **2011**, *158*, A1011.
[23] Y. Mo, S. P. Ong, G. Ceder, *Chem. Mater.* **2014**, *26*, 5208.
[24] S. T. Dacek, W. D. Richards, D. A. Kitchaev, G. Ceder, *Chem. Mater.* **2016**, *28*, 5450.
[25] H. Chen, G. Hautier, G. Ceder, *J. Am. Chem. Soc.* **2012**, *134*, 19619.
[26] H. Chen, Q. Hao, O. Zivkovic, G. Hautier, L.-S. Du, Y. Tang, Y.-Y. Hu, X. Ma, C. P. Grey, G. Ceder, *Chem. Mater.* **2013**, *25*, 2777.
[27] Y. Wang, W. D. Richards, S.-H. Bo, L. J. Miara, G. Ceder, *Chem. Mater.* **2017**, *29*, 7475.
[28] S.-H. Bo, X. Li, A. J. Toumar, G. Ceder, *Chem. Mater.* **2016**, *28*, 1419.
[29] W. D. Richards, T. Tsujimura, L. J. Miara, Y. Wang, J. C. Kim, S. P. Ong, I. Uechi, N. Suzuki, G. Ceder, *Nat. Commun.* **2016**, *7*, 11009.
[30] S.-H. Bo, Y. Wang, G. Ceder, *J. Mater. Chem. A* **2016**, *4*, 9044.
[31] D. Wu, X. Li, B. Xu, N. Twu, L. Liu, G. Ceder, *Energy Environ. Sci.* **2015**, *8*, 195.
[32] G. Hautier, A. Jain, H. Chen, C. Moore, S. P. Ong, G. Ceder, *J. Mater. Chem.* **2011**, *21*, 17147.
[33] G. Hautier, A. Jain, S. P. Ong, B. Kang, C. Moore, R. Doe, G. Ceder, *Chem. Mater.* **2011**, *23*, 3495.
[34] M. Guignard, C. Didier, J. Darriet, P. Bordet, E. Elkaïm, C. Delmas, *Nat. Mater.* **2013**, *12*, 74.
[35] R. Berthelot, D. Carlier, C. Delmas, *Nat. Mater.* **2011**, *10*, 74.
[36] Y. Hinuma, Y. S. Meng, G. Ceder, *Phys. Rev. B* **2008**, *77*, 224111.
[37] A. J. Toumar, S. P. Ong, W. D. Richards, S. Dacek, G. Ceder, *Phys. Rev. Appl.* **2015**, *4*, 064002.
[38] C. Zheng, B. Radhakrishnan, I.-H. Chu, Z. Wang, S. P. Ong, *Phys. Rev. Appl.* **2017**, *7*, 064003.

[39] Z. Deng, Y. Mo, S. P. Ong, *NPG Asia Mater.* **2016**, *8*, e254.
[40] M. S. Islam, C. A. J. Fisher, *Chem. Soc. Rev.* **2014**, *43*, 185.
[41] Y. S. Meng, M. E. Arroyo-de Dompablo, *Acc. Chem. Res.* **2012**, *46*, 1171.
[42] A. Urban, D.-H. Seo, G. Ceder, *npj Comput. Mater.* **2016**, *2*, 16002.
[43] Y. S. Meng, Y. Hinuma, G. Ceder, *J. Chem. Phys.* **2008**, *128*, 104708.
[44] T. R. Jow, L. W. Shacklette, M. Maxfield, D. Vernick, *J. Electrochem. Soc.* **1987**, *134*, 1730.
[45] H. Kim, D. J. Kim, D.-H. Seo, M. S. Yeom, K. Kang, D. K. Kim, Y. Jung, *Chem. Mater.* **2012**, *24*, 1205.
[46] G. Hautier, C. C. Fischer, A. Jain, T. Mueller, G. Ceder, *Chem. Mater.* **2010**, *22*, 3762.
[47] A. Van der Ven, M. K. Aydinol, G. Ceder, G. Kresse, J. Hafner, *Phys. Rev. B* **1998**, *58*, 2975.
[48] M. A. y de Dompablo, A. Van der Ven, G. Ceder, *Phys. Rev. B* **2002**, *66*, 064112.
[49] A. I. Liechtenstein, V. I. Anisimov, J. Zaanen, *Phys. Rev. B* **1995**, *52*, R5467.
[50] M. Cococcioni, S. De Gironcoli, *Phys. Rev. B* **2005**, *71*, 035105.
[51] V. I. Anisimov, J. Zaanen, O. K. Andersen, *Phys. Rev. B* **1991**, *44*, 943.
[52] V. I. Anisimov, F. Aryasetiawan, A. I. Lichtenstein, *J. Phys.: Condens. Matter* **1997**, *9*, 767.
[53] S. L. Dudarev, G. A. Botton, S. Y. Savrasov, C. J. Humphreys, A. P. Sutton, *Phys. Rev. B* **1998**, *57*, 1505.
[54] H. J. Kulik, M. Cococcioni, D. A. Scherlis, N. Marzari, *Phys. Rev. Lett.* **2006**, *97*, 103001.
[55] F. Zhou, M. Cococcioni, C. A. Marianetti, D. Morgan, G. Ceder, *Phys. Rev. B* **2004**, *70*, 235121.
[56] L. Wang, T. Maxisch, G. Ceder, *Phys. Rev. B* **2006**, *73*, 195107.
[57] M. B. Yahia, F. Lemoigno, G. Rousse, F. Boucher, J.-M. Tarascon, M.-L. Doublet, *Energy Environ. Sci.* **2012**, *5*, 9584.
[58] F. Zhou, K. Kang, T. Maxisch, G. Ceder, D. Morgan, *Solid State Commun.* **2004**, *132*, 181.
[59] J. Klimeš, A. Michaelides, *J. Chem. Phys.* **2012**, *137*, 120901.
[60] K. Berland, V. R. Cooper, K. Lee, E. Schröder, T. Thonhauser, P. Hyldgaard, B. I. Lundqvist, *Rep. Prog. Phys.* **2015**, *78*, 066501.
[61] Z. Wang, S. M. Selbach, T. Grande, *RSC Adv.* **2014**, *4*, 4069.
[62] G.-C. Ri, C.-J. Yu, J.-S. Kim, S.-N. Hong, U.-G. Jong, M.-H. Ri, *J. Power Sources* **2016**, *324*, 758.
[63] P.-c. Tsai, S.-C. Chung, S.-k. Lin, A. Yamada, *J. Mater. Chem. A* **2015**, *3*, 9763.
[64] V. V. Kulish, O. I. Malyi, C. Persson, P. Wu, *Phys. Chem. Chem. Phys.* **2015**, *17*, 13921.
[65] V. V. Kulish, O. I. Malyi, M.-F. Ng, Z. Chen, S. Manzhos, P. Wu, *Phys. Chem. Chem. Phys.* **2014**, *16*, 4260.
[66] T. Yamashita, H. Momida, T. Oguchi, *Electrochim. Acta* **2016**, *195*, 1.
[67] R. B. Araujo, A. Banerjee, R. Ahuja, *J. Phys. Chem. C* **2017**, *121*, 14027.
[68] S. Grimme, *J. Comput. Chem.* **2004**, *25*, 1463.
[69] S. Grimme, *J. Comput. Chem.* **2006**, *27*, 1787.
[70] S. Grimme, J. Antony, S. Ehrlich, H. Krieg, *J. Chem. Phys.* **2010**, *132*, 154104.
[71] M. Dion, H. Rydberg, E. Schröder, D. C. Langreth, B. I. Lundqvist, *Phys. Rev. Lett.* **2004**, *92*, 246401.
[72] O. A. Vydrov, T. Van Voorhis, *J. Chem. Phys.* **2010**, *133*, 244103.
[73] J. Klimeš, D. R. Bowler, A. Michaelides, *J. Phys.: Condens. Matter* **2009**, *22*, 022201.
[74] G. Mills, H. Jónsson, G. K. Schenter, *Surf. Sci.* **1995**, *324*, 305.
[75] G. Henkelman, B. P. Uberuaga, H. Jónsson, *J. Chem. Phys.* **2000**, *113*, 9901.
[76] I. L. Matts, S. Dacek, T. K. Pietrzak, R. Malik, G. Ceder, *Chem. Mater.* **2015**, *27*, 6008.
[77] X. He, Y. Zhu, Y. Mo, *Nat. Commun.* **2017**, *8*, 15893.
[78] A. Van der Ven, G. Ceder, M. Asta, P. D. Tepesch, *Phys. Rev. B* **2001**, *64*, 184307.
[79] R. Tripathi, S. M. Wood, M. S. Islam, L. F. Nazar, *Energy Environ. Sci.* **2013**, *6*, 2257.
[80] Y. Mo, S. P. Ong, G. Ceder, *Chem. Mater.* **2011**, *24*, 15.
[81] S. P. Ong, Y. Mo, W. D. Richards, L. Miara, H. S. Lee, G. Ceder, *Energy Environ. Sci.* **2013**, *6*, 148.
[82] W. J. Li, C. Han, W. Wang, F. Gebert, S. L. Chou, H. K. Liu, X. Zhang, S. X. Dou, *Adv. Energy Mater.* **2017**, *7*, 1700274.
[83] B. L. Ellis, K. T. Lee, L. F. Nazar, *Chem. Mater.* **2010**, *22*, 691.
[84] M. H. Han, E. Gonzalo, G. Singh, T. Rojo, *Energy Environ. Sci.* **2015**, *8*, 81.
[85] X. Li, D. Wu, Y.-N. Zhou, L. Liu, X.-Q. Yang, G. Ceder, *Electrochem. Commun.* **2014**, *49*, 51.
[86] C. Didier, M. Guignard, C. Denage, O. Szajwaj, S. Ito, I. Saadoune, J. Darriet, C. Delmas, *Electrochem. Solid-State Lett.* **2011**, *14*, A75.
[87] C. Delmas, C. Fouassier, P. Hagenmuller, *Physica B+C* **1980**, *99*, 81.
[88] K. Mizushima, P. C. Jones, P. J. Wiseman, J. B. Goodenough, *Mater. Res. Bull.* **1980**, *15*, 783.
[89] K. M. Shaju, G. V. S. Rao, B. V. R. Chowdari, *Electrochim. Acta* **2002**, *48*, 145.
[90] N. Yabuuchi, R. Hara, K. Kubota, J. Paulsen, S. Kumakura, S. Komaba, *J. Mater. Chem. A* **2014**, *2*, 16851.
[91] X. Wang, M. Tamaru, M. Okubo, A. Yamada, *J. Phys. Chem. C* **2013**, *117*, 15545.
[92] G. Ceder, P. D. Tepesch, A. F. Kohan, A. Van der Ven, *J. Electroceram.* **1997**, *1*, 15.
[93] C. Didier, M. Guignard, J. Darriet, C. Delmas, *Inorg. Chem.* **2012**, *51*, 11007.
[94] X. Li, X. Ma, D. Su, L. Liu, R. Chisnell, S. P. Ong, H. Chen, A. Toumar, J.-C. Idrobo, Y. Lei, *Nat. Mater.* **2014**, *13*, 586.
[95] F. Zhou, T. Maxisch, G. Ceder, *Phys. Rev. Lett.* **2006**, *97*, 155704.
[96] J.-J. Ding, Y.-N. Zhou, Q. Sun, Z.-W. Fu, *Electrochem. Commun.* **2012**, *22*, 85.
[97] J. J. Ding, Y. N. Zhou, Q. Sun, X. Q. Yu, X. Q. Yang, Z. W. Fu, *Electrochim. Acta* **2013**, *87*, 388.
[98] A. Van der Ven, G. Ceder, *Electrochem. Solid-State Lett.* **2000**, *3*, 301.
[99] G. Li, X. Yue, G. Luo, J. Zhao, *Comput. Mater. Sci.* **2015**, *106*, 15.
[100] S. Kim, X. Ma, S. P. Ong, G. Ceder, *Phys. Chem. Chem. Phys.* **2012**, *14*, 15571.
[101] K. Kubota, T. Asari, H. Yoshida, N. Yaabuuchi, H. Shiiba, M. Nakayama, S. Komaba, *Adv. Funct. Mater.* **2016**, *26*, 6047.
[102] L. A. De Picciotto, M. M. Thackeray, *Mater. Res. Bull.* **1985**, *20*, 187.
[103] Y. Shao-Horn, S. A. Hackney, A. R. Armstrong, P. G. Bruce, R. Gitzendanner, C. S. Johnson, M. M. Thackeray, *J. Electrochem. Soc.* **1999**, *146*, 2404.
[104] M. G. S. R. Thomas, W. I. F. David, J. B. Goodenough, P. Groves, *Mater. Res. Bull.* **1985**, *20*, 1137.
[105] R. Alcantara, P. Lavela, J. L. Tirado, E. Zhecheva, R. Stoyanova, *J. Electroanal. Chem.* **1998**, *454*, 173.
[106] H. Gabrisch, R. Yazami, B. Fultz, *J. Electrochem. Soc.* **2004**, *151*, A891.
[107] K. Kang, G. Ceder, *Phys. Rev. B* **2006**, *74*, 094105.
[108] Y.-M. Choi, S.-I. Pyun, S.-I. Moon, *Solid State Ionics* **1996**, *89*, 43.
[109] J. Reed, G. Ceder, *Chem. Rev.* **2004**, *104*, 4513.
[110] S. A. Magarill, S. V. Borisov, N. V. Podberezskaya, E. N. Ipatova, V. A. Titov, F. A. Kuznetsov, *J. Struct. Chem.* **1995**, *36*, 510.
[111] R. D. Shannon, *Acta Crystallogr., Sect. A: Cryst. Phys., Diffr., Theor. Gen. Crystallogr.* **1976**, *A32*, 751.
[112] Z. Chen, Z. Lu, J. R. Dahn, *J. Electrochem. Soc.* **2002**, *149*, A1604.
[113] J. Vinckevičiūtė, M. D. Radin, A. Van der Ven, *Chem. Mater.* **2016**, *28*, 8640.
[114] H. Gabrisch, R. Yazami, B. Fultz, *Electrochem. Solid-State Lett.* **2002**, *5*, A111.

[115] X. Lu, G. Xia, J. P. Lemmon, Z. Yang, *J. Power Sources* **2010**, *195*, 2431.
[116] P. Zhang, R. B. Capaz, M. L. Cohen, S. G. Louie, *Phys. Rev. B* **2005**, *71*, 153102.
[117] Y. Wang, J. Ni, *Phys. Rev. B* **2007**, *76*, 094101.
[118] M. Roger, D. J. P. Morris, D. A. Tennant, M. J. Gutmann, J. P. Goff, J. U. Hoffmann, R. Feyerherm, E. Dudzik, D. Prabhakaran, A. T. Boothroyd, N. Shannon, B. Lake, P. P. Deen, *Nature* **2007**, *445*, 631.
[119] Q. Huang, M. L. Foo, J. W. Lynn, H. W. Zandbergen, G. Lawes, Y. Wang, B. H. Toby, A. P. Ramirez, N. P. Ong, R. J. Cava, *J. Phys.: Condens. Matter* **2004**, *16*, 5803.
[120] H. W. Zandbergen, M. Foo, Q. Xu, V. Kumar, R. J. Cava, *Phys. Rev. B* **2004**, *70*, 024101.
[121] Q. Huang, M. L. Foo, R. A. Pascal Jr., J. W. Lynn, B. H. Toby, T. He, H. W. Zandbergen, R. J. Cava, *Phys. Rev. B* **2004**, *70*, 184110.
[122] R. J. Balsys, R. L. Davis, *Solid State Ionics* **1997**, *93*, 279.
[123] I. R. Mukhamedshin, H. Alloul, G. Collin, N. Blanchard, *Phys. Rev. Lett.* **2004**, *93*, 167601.
[124] Y. S. Meng, A. Van der Ven, M. K. Y. Chan, G. Ceder, *Phys. Rev. B* **2005**, *72*, 172103.
[125] J. Geck, M. v. Zimmermann, H. Berger, S. V. Borisenko, H. Eschrig, K. Koepernik, M. Knupfer, B. Büchner, *Phys. Rev. Lett.* **2006**, *97*, 106403.
[126] D. Kim, S. H. Kang, M. Slater, S. Rood, J. T. Vaughey, N. Karan, M. Balasubramanian, C. S. Johnson, *Adv. Energy Mater.* **2011**, *1*, 333.
[127] J. Xu, D. H. Lee, R. l. J. Clément, X. Yu, M. Leskes, A. J. Pell, G. Pintacuda, X.-Q. Yang, C. P. Grey, Y. S. Meng, *Chem. Mater.* **2014**, *26*, 1260.
[128] S. Doubaji, M. Valvo, I. Saadoune, M. Dahbi, K. Edström, *J. Power Sources* **2014**, *266*, 275.
[129] D. H. Lee, J. Xu, Y. S. Meng, *Phys. Chem. Chem. Phys.* **2013**, *15*, 3304.
[130] T. Shibata, W. Kobayashi, Y. Moritomo, *Appl. Phys. Express* **2014**, *7*, 067101.
[131] N. A. Katcho, J. Carrasco, D. Saurel, E. Gonzalo, M. Han, F. Aguesse, T. Rojo, *Adv. Energy Mater.* **2017**, *7*, 1601477.
[132] T. Shibata, Y. Fukuzumi, W. Kobayashi, Y. Moritomo, *Sci. Rep.* **2015**, *5*, 9006.
[133] Y. Lei, X. Li, L. Liu, G. Ceder, *Chem. Mater.* **2014**, *26*, 5288.
[134] C. Masquelier, L. Croguennec, *Chem. Rev.* **2013**, *113*, 6552.
[135] A. Saracibar, J. Carrasco, D. Saurel, M. Galceran, B. Acebedo, H. Anne, M. Lepoitevin, T. Rojo, M. C. Cabanas, *Phys. Chem. Chem. Phys.* **2016**, *18*, 13045.
[136] P. Moreau, D. Guyomard, J. Gaubicher, F. Boucher, *Chem. Mater.* **2010**, *22*, 4126.
[137] K. T. Lee, T. N. Ramesh, F. Nan, G. Botton, L. F. Nazar, *Chem. Mater.* **2011**, *23*, 3593.
[138] M. Galceran, D. Saurel, B. Acebedo, V. V. Roddatis, E. Martin, T. Rojo, M. Casas-Cabanas, *Phys. Chem. Chem. Phys.* **2014**, *16*, 8837.
[139] M. Galceran, V. Roddatis, F. J. Zúñiga, J. M. Pérez-Mato, B. Acebedo, R. Arenal, I. Peral, T. Rojo, M. Casas-Cabanas, *Chem. Mater.* **2014**, *26*, 3289.
[140] F. Boucher, J. Gaubicher, M. Cuisinier, D. Guyomard, P. Moreau, *J. Am. Chem. Soc.* **2014**, *136*, 9144.
[141] J. Lu, S. C. Chung, S.-i. Nishimura, A. Yamada, *Chem. Mater.* **2013**, *25*, 4557.
[142] C. Li, X. Miao, W. Chu, P. Wu, D. G. Tong, *J. Mater. Chem. A* **2015**, *3*, 8265.
[143] J. Kim, D.-H. Seo, H. Kim, I. Park, J.-K. Yoo, S.-K. Jung, Y.-U. Park, W. A. Goddard III, K. Kang, *Energy Environ. Sci.* **2015**, *8*, 540.
[144] J. N. Bridson, S. E. Quinlan, P. R. Tremaine, *Chem. Mater.* **1998**, *10*, 763.
[145] P. R. Tremaine, C. Xiao, *J. Chem. Thermodyn.* **1999**, *31*, 1307.
[146] M. Casas-Cabanas, V. V. Roddatis, D. Saurel, P. Kubiak, J. Carretero-González, V. Palomares, P. Serras, T. Rojo, *J. Mater. Chem.* **2012**, *22*, 17421.
[147] M. Nakayama, S. Yamada, R. Jalem, T. Kasuga, *Solid State Ionics* **2016**, *286*, 40.
[148] R. Malik, D. Burch, M. Bazant, G. Ceder, *Nano Lett.* **2010**, *10*, 4123.
[149] C. A. J. Fisher, V. M. Hart Prieto, M. S. Islam, *Chem. Mater.* **2008**, *20*, 5907.
[150] M. S. Islam, D. J. Driscoll, C. A. J. Fisher, P. R. Slater, *Chem. Mater.* **2005**, *17*, 5085.
[151] X. Wu, J. Zheng, Z. Gong, Y. Yang, *J. Mater. Chem.* **2011**, *21*, 18630.
[152] Y. Zheng, P. Zhang, S. Q. Wu, Y. H. Wen, Z. Z. Zhu, Y. Yang, *J. Electrochem. Soc.* **2013**, *160*, A927.
[153] Q. Ni, Y. Bai, F. Wu, C. Wu, *Adv. Sci.* **2017**, *4*, 2198.
[154] Y. Kawabe, N. Yabuuchi, M. Kajiyama, N. Fukuhara, T. Inamasu, R. Okuyama, I. Nakai, S. Komaba, *Electrochem. Commun.* **2011**, *13*, 1225.
[155] N. Recham, J.-N. Chotard, L. Dupont, K. Djellab, M. Armand, J.-M. Tarascon, *J. Electrochem. Soc.* **2009**, *156*, A993.
[156] O. V. Yakubovich, O. V. Karimova, O. K. Mel'nikov, *Acta Crystallogr., Sect. C: Cryst. Struct. Commun.* **1997**, *53*, 395.
[157] F. Sanz, C. Parada, C. Ruíz-Valero, *J. Mater. Chem.* **2001**, *11*, 208.
[158] S.-W. Kim, D.-H. Seo, H. Kim, K.-Y. Park, K. Kang, *Phys. Chem. Chem. Phys.* **2012**, *14*, 3299.
[159] Y. Zhong, Z. Wu, Y. Tang, W. Xiang, X. Guo, B. Zhong, *Mater. Lett.* **2015**, *145*, 269.
[160] X. Lin, X. Hou, X. Wu, S. Wang, M. Gao, Y. Yang, *RSC Adv.* **2014**, *4*, 40985.
[161] B. L. Ellis, W. R. M. Makahnouk, W. N. Rowan-Weetaluktuk, D. H. Ryan, L. F. Nazar, *Chem. Mater.* **2009**, *22*, 1059.
[162] Y. Kawabe, N. Yabuuchi, M. Kajiyama, N. Fukuhara, T. Inamasu, R. Okuyama, I. Nakai, S. Komaba, *Electrochemistry* **2012**, *80*, 80.
[163] Y. Zhu, Y. Xu, Y. Liu, C. Luo, C. Wang, *Nanoscale* **2013**, *5*, 780.
[164] J. M. Le Meins, M. P. Crosnier-Lopez, A. Hemon-Ribaud, G. Courbion, *J. Solid State Chem.* **1999**, *148*, 260.
[165] R. A. Shakoor, D.-H. Seo, H. Kim, Y.-U. Park, J. Kim, S.-W. Kim, H. Gwon, S. Lee, K. Kang, *J. Mater. Chem.* **2012**, *22*, 20535.
[166] Y. U. Park, D. H. Seo, H. Kim, J. Kim, S. Lee, B. Kim, K. Kang, *Adv. Funct. Mater.* **2014**, *24*, 4603.
[167] M. Bianchini, F. Fauth, N. Brisset, F. Weill, E. Suard, C. Masquelier, L. Croguennec, *Chem. Mater.* **2015**, *27*, 3009.
[168] M. Bianchini, N. Brisset, F. Fauth, F. Weill, E. Elkaim, E. Suard, C. Masquelier, L. Croguennec, *Chem. Mater.* **2014**, *26*, 4238.
[169] M. Xu, P. Xiao, S. Stauffer, J. Song, G. Henkelman, J. B. Goodenough, *Chem. Mater.* **2014**, *26*, 3089.
[170] A. Ponrouch, E. Marchante, M. Courty, J.-M. Tarascon, M. R. Palacin, *Energy Environ. Sci.* **2012**, *5*, 8572.
[171] R. K. B. Gover, A. Bryan, P. Burns, J. Barker, *Solid State Ionics* **2006**, *177*, 1495.
[172] Z. Liu, Y.-Y. Hu, M. T. Dunstan, H. Huo, X. Hao, H. Zou, G. Zhong, Y. Yang, C. P. Grey, *Chem. Mater.* **2014**, *26*, 2513.
[173] P. Barpanda, T. Ye, S.-i. Nishimura, S.-C. Chung, Y. Yamada, M. Okubo, H. Zhou, A. Yamada, *Electrochem. Commun.* **2012**, *24*, 116.
[174] P. Barpanda, T. Ye, M. Avdeev, S.-C. Chung, A. Yamada, *J. Mater. Chem. A* **2013**, *1*, 4194.
[175] M. Chen, L. Chen, Z. Hu, Q. Liu, B. Zhang, Y. Hu, Q. Gu, J. L. Wang, L. Z. Wang, X. Guo, S. L. Chou, S. X. Dou, *Adv. Mater.* **2017**, *29*, 1605535.
[176] C. S. Park, H. Kim, R. A. Shakoor, E. Yang, S. Y. Lim, R. Kahraman, Y. Jung, J. W. Choi, *J. Am. Chem. Soc.* **2013**, *135*, 2787.
[177] S. Y. Lim, H. Kim, J. Chung, J. H. Lee, B. G. Kim, J. J. Choi, K. Y. Chung, W. Cho, S. J. Kim, W. A. Goddard 3rd, Y. Jung, J. W. Choi, *Proc. Natl. Acad. Sci. USA* **2014**, *111*, 599.

[178] H. Kim, R. A. Shakoor, C. Park, S. Y. Lim, J.-S. Kim, Y. N. Jo, W. Cho, K. Miyasaka, R. Kahraman, Y. Jung, J. W. Choi, *Adv. Funct. Mater.* **2013**, *23*, 1147.
[179] H. Kim, C. S. Park, J. W. Choi, Y. Jung, *Angew. Chem., Int. Ed.* **2016**, *55*, 6662.
[180] H. Kim, G. Yoon, I. Park, K.-Y. Park, B. Lee, J. Kim, Y.-U. Park, S.-K. Jung, H.-D. Lim, D. Ahn, S. Lee, K. Kang, *Energy Environ. Sci.* **2015**, *8*, 3325.
[181] H. Kim, I. Park, S. Lee, H. Kim, K.-Y. Park, Y.-U. Park, H. Kim, J. Kim, H.-D. Lim, W.-S. Yoon, *Chem. Mater.* **2013**, *25*, 3614.
[182] M. Reynaud, G. Rousse, A. M. Abakumov, M. T. Sougrati, G. Van Tendeloo, J.-N. Chotard, J.-M. Tarascon, *J. Mater. Chem. A* **2014**, *2*, 2671.
[183] P. Singh, K. Shiva, H. Celio, J. B. Goodenough, *Energy Environ. Sci.* **2015**, *8*, 3000.
[184] P. Barpanda, G. Oyama, S. Nishimura, S. C. Chung, A. Yamada, *Nat. Commun.* **2014**, *5*, 4358.
[185] W. Huang, J. Zhou, B. Li, J. Ma, S. Tao, D. Xia, W. Chu, Z. Wu, *Sci. Rep.* **2014**, *4*, 4188.
[186] A. Jain, G. Hautier, C. J. Moore, S. P. Ong, C. C. Fischer, T. Mueller, K. A. Persson, G. Ceder, *Comput. Mater. Sci.* **2011**, *50*, 2295.
[187] Z. Wang, I.-H. Chu, F. Zhou, S. P. Ong, *Chem. Mater.* **2016**, *28*, 4024.
[188] Z. Jian, Y. S. Hu, X. Ji, W. Chen, *Adv. Mater.* **2017**, *29*, 1601925.
[189] S. Y. Lim, H. Kim, R. A. Shakoor, Y. Jung, J. W. Choi, *J. Electrochem. Soc.* **2012**, *159*, A1393.
[190] K. M. Bui, V. A. Dinh, S. Okada, T. Ohno, *Phys. Chem. Chem. Phys.* **2015**, *17*, 30433.
[191] X. Rui, W. Sun, C. Wu, Y. Yu, Q. Yan, *Adv. Mater.* **2015**, *27*, 6670.
[192] Z. Jian, W. Han, X. Lu, H. Yang, Y. S. Hu, J. Zhou, Z. Zhou, J. Li, W. Chen, D. Chen, *Adv. Energy Mater.* **2013**, *3*, 156.
[193] Y. Fang, L. Xiao, X. Ai, Y. Cao, H. Yang, *Adv. Mater.* **2015**, *27*, 5895.
[194] Z. Jian, Y. Sun, X. Ji, *Chem. Commun.* **2015**, *51*, 6381.
[195] J. Gaubicher, C. Wurm, G. Goward, C. Masquelier, L. Nazar, *Chem. Mater.* **2000**, *12*, 3240.
[196] D. Morgan, G. Ceder, M. Y. Saidi, J. Barker, J. Swoyer, H. Huang, G. Adamson, *Chem. Mater.* **2002**, *14*, 4684.
[197] H. Chen, M. Armand, G. Demailly, F. Dolhem, P. Poizot, J. M. Tarascon, *ChemSusChem* **2008**, *1*, 348.
[198] K. Chihara, N. Chujo, A. Kitajou, S. Okada, *Electrochim. Acta* **2013**, *110*, 240.
[199] H. Kim, J. E. Kwon, B. Lee, J. Hong, M. Lee, S. Y. Park, K. Kang, *Chem. Mater.* **2015**, *27*, 7258.
[200] Q. Zhao, Y. Lu, J. Chen, *Adv. Energy Mater.* **2017**, *7*, 1601792.
[201] Y. Xu, M. Zhou, Y. Lei, *Mater. Today* **2017**, https://doi.org/10.1016/j.mattod.2017.07.005.
[202] X. Wu, S. Jin, Z. Zhang, L. Jiang, L. Mu, Y.-S. Hu, H. Li, X. Chen, M. Armand, L. Chen, *Sci. Adv.* **2015**, *1*, e1500330.
[203] A. R. Oganov, C. W. Glass, *J. Chem. Phys.* **2006**, *124*, 244704.
[204] A. R. Oganov, A. O. Lyakhov, M. Valle, *Acc. Chem. Res.* **2011**, *44*, 227.
[205] A. O. Lyakhov, A. R. Oganov, H. T. Stokes, Q. Zhu, *Comput. Phys. Commun.* **2013**, *184*, 1172.
[206] Y. Chen, J. Lüder, M.-F. Ng, M. B. Sullivan, S. Manzhos, *Phys. Chem. Chem. Phys.* **2017**, *20*, 232.
[207] Y. Chen, S. Manzhos, *Phys. Chem. Chem. Phys.* **2016**, *18*, 8874.
[208] P. Ge, M. Fouletier, *Solid State Ionics* **1988**, *28*, 1172.
[209] V. Palomares, P. Serras, I. Villaluenga, K. B. Hueso, J. Carretero-González, T. Rojo, *Energy Environ. Sci.* **2012**, *5*, 5884.
[210] M. D. Slater, D. Kim, E. Lee, C. S. Johnson, *Adv. Funct. Mater.* **2013**, *23*, 947.
[211] D. A. Stevens, J. R. Dahn, *J. Electrochem. Soc.* **2001**, *148*, A803.
[212] Y. Liu, B. V. Merinov, W. A. Goddard, *Proc. Natl. Acad. Sci. USA* **2016**, *113*, 3735.
[213] Y. Cao, L. Xiao, M. L. Sushko, W. Wang, B. Schwenzer, J. Xiao, Z. Nie, L. V. Saraf, Z. Yang, J. Liu, *Nano Lett.* **2012**, *12*, 3783.
[214] D. Aurbach, M. D. Levi, E. Levi, H. Teller, B. Markovsky, G. Salitra, U. Heider, L. Heider, *J. Electrochem. Soc.* **1998**, *145*, 3024.
[215] Y. F. Reynier, R. Yazami, B. Fultz, *J. Electrochem. Soc.* **2004**, *151*, A422.
[216] R. Raccichini, A. Varzi, S. Passerini, B. Scrosati, *Nat. Mater.* **2015**, *14*, 271.
[217] M. S. Dresselhaus, G. Dresselhaus, *Adv. Phys.* **1981**, *30*, 139.
[218] Y. Okamoto, *J. Phys. Chem. C* **2013**, *118*, 16.
[219] D. A. Stevens, J. R. Dahn, *J. Electrochem. Soc.* **2000**, *147*, 4428.
[220] Y.-X. Wang, S.-L. Chou, H.-K. Liu, S.-X. Dou, *Carbon* **2013**, *57*, 202.
[221] J. Ding, H. Wang, Z. Li, A. Kohandehghan, K. Cui, Z. Xu, B. Zahiri, X. Tan, E. M. Lotfabad, B. C. Olsen, *ACS Nano* **2013**, *7*, 11004.
[222] E. Irisarri, A. Ponrouch, M. R. Palacin, *J. Electrochem. Soc.* **2015**, *162*, A2476.
[223] J.-Y. Hwang, S.-T. Myung, Y.-K. Sun, *Chem. Soc. Rev.* **2017**, *46*, 3529.
[224] M. Lao, Y. Zhang, W. Luo, Q. Yan, W. Sun, S. X. Dou, *Adv. Mater.* **2017**, *29*, 1521.
[225] Y. Kim, Y. Park, A. Choi, N. S. Choi, J. Kim, J. Lee, J. H. Ryu, S. M. Oh, K. T. Lee, *Adv. Mater.* **2013**, *25*, 3045.
[226] M. Mortazavi, Q. Ye, N. Birbilis, N. V. Medhekar, *J. Power Sources* **2015**, *285*, 29.
[227] N. Yabuuchi, Y. Matsuura, T. Ishikawa, S. Kuze, J. Y. Son, Y. T. Cui, H. Oji, S. Komaba, *ChemElectroChem* **2014**, *1*, 580.
[228] L. D. Ellis, B. N. Wilkes, T. D. Hatchard, M. N. Obrovac, *J. Electrochem. Soc.* **2014**, *161*, A416.
[229] A. Darwiche, C. Marino, M. T. Sougrati, B. Fraisse, L. Stievano, L. Monconduit, *J. Am. Chem. Soc.* **2012**, *134*, 20805.
[230] C.-Y. Chou, M. Lee, G. S. Hwang, *J. Phys. Chem. C* **2015**, *119*, 14843.
[231] J. W. Wang, X. H. Liu, S. X. Mao, J. Y. Huang, *Nano Lett.* **2012**, *12*, 5897.
[232] S. C. Jung, D. S. Jung, J. W. Choi, Y.-K. Han, *J. Phys. Chem. Lett.* **2014**, *5*, 1283.
[233] H. Morito, T. Yamada, T. Ikeda, H. Yamane, *J. Alloys Compd.* **2009**, *480*, 723.
[234] J. Sangster, A. D. Pelton, *J. Phase Equilib.* **1997**, *18*, 295.
[235] A. Kohandehghan, K. Cui, M. Kupsta, J. Ding, E. Memarzadeh Lotfabad, W. P. Kalisvaart, D. Mitlin, *Nano Lett.* **2014**, *14*, 5873.
[236] L. Baggetto, J. K. Keum, J. F. Browning, G. M. Veith, *Electrochem. Commun.* **2013**, *34*, 41.
[237] C. Yue, Y. Yu, S. Sun, X. He, B. Chen, W. Lin, B. Xu, M. Zheng, S. Wu, J. Li, *Adv. Funct. Mater.* **2015**, *25*, 1386.
[238] O. I. Malyi, T. L. Tan, S. Manzhos, *Appl. Phys. Express* **2013**, *6*, 027301.
[239] J. Sun, H.-W. Lee, M. Pasta, H. Yuan, G. Zheng, Y. Sun, Y. Li, Y. Cui, *Nat. Nanotechnol.* **2015**, *10*, 980.
[240] T. Ramireddy, T. Xing, M. M. Rahman, Y. Chen, Q. Dutercq, D. Gunzelmann, A. M. Glushenkov, *J. Mater. Chem. A* **2015**, *3*, 5572.
[241] J. Song, Z. Yu, M. L. Gordin, X. Li, H. Peng, D. Wang, *ACS Nano* **2015**, *9*, 11933.
[242] S. Yao, J. Cui, J. Huang, J. Q. Huang, W. G. Chong, L. Qin, Y. W. Mai, J. K. Kim, *Adv. Energy Mater.* **2017**, https://doi.org/10.1002/aenm.201702267.
[243] J. Cui, S. Yao, J.-K. Kim, *Energy Storage Mater.* **2017**, *7*, 64.
[244] Y. Li, Y. Lu, C. Zhao, Y.-S. Hu, M.-M. Titirici, H. Li, X. Huang, L. Chen, *Energy Storage Mater.* **2017**, *7*, 130.
[245] M. Mayo, K. J. Griffith, C. J. Pickard, A. J. Morris, *Chem. Mater.* **2016**, *28*, 2011.
[246] K. Hembram, H. Jung, B. C. Yeo, S. J. Pai, S. Kim, K.-R. Lee, S. S. Han, *J. Phys. Chem. C* **2015**, *119*, 15041.
[247] X.-f. Yu, H. Ushiyama, K. Yamashita, *Chem. Lett.* **2014**, *43*, 1940.

[248] X.-f. Yu, G. Giorgi, H. Ushiyama, K. Yamashita, *Chem. Phys. Lett.* **2014**, *612*, 129.
[249] K. P. S. S. Hembram, H. Jung, B. C. Yeo, S. J. Pai, H. J. Lee, K.-R. Lee, S. S. Han, *Phys. Chem. Chem. Phys.* **2016**, *18*, 21391.
[250] D. A. Stevens, J. R. Dahn, *J. Electrochem. Soc.* **2000**, *147*, 1271.
[251] M. N. Obrovac, L. Christensen, D. B. Le, J. R. Dahn, *J. Electrochem. Soc.* **2007**, *154*, A849.
[252] M. Mortazavi, J. Deng, V. B. Shenoy, N. V. Medhekar, *J. Power Sources* **2013**, *225*, 207.
[253] B. Farbod, K. Cui, W. P. Kalisvaart, M. Kupsta, B. Zahiri, A. Kohandehghan, E. M. Lotfabad, Z. Li, E. J. Luber, D. Mitlin, *ACS Nano* **2014**, *8*, 4415.
[254] F. Klein, B. Jache, A. Bhide, P. Adelhelm, *Phys. Chem. Chem. Phys.* **2013**, *15*, 15876.
[255] P. R. Kumar, Y. H. Jung, K. K. Bharathi, C. H. Lim, D. K. Kim, *Electrochim. Acta* **2014**, *146*, 503.
[256] L.-L. Feng, G.-D. Li, Y. Liu, Y. Wu, H. Chen, Y. Wang, Y.-C. Zou, D. Wang, X. Zou, *ACS Appl. Mater. Interfaces* **2015**, *7*, 980.
[257] J. Fullenwarth, A. Darwiche, A. Soares, B. Donnadieu, L. Monconduit, *J. Mater. Chem. A* **2014**, *2*, 2050.
[258] Z. Hu, Q. Liu, S. L. Chou, S. X. Dou, *Adv. Mater.* **2017**, *29*, 1700606.
[259] Y. Xiao, S. H. Lee, Y. K. Sun, *Adv. Energy Mater.* **2017**, *7*, 1601329.
[260] X. Xiong, G. Wang, Y. Lin, Y. Wang, X. Ou, F. Zheng, C. Yang, J. H. Wang, M. Liu, *ACS Nano* **2016**, *10*, 10953.
[261] S. Yao, J. Cui, Z. Lu, Z.-L. Xu, L. Qin, J. Huang, Z. Sadighi, F. Ciucci, J.-K. Kim, *Adv. Energy Mater.* **2017**, *7*, 1602149.
[262] K. He, F. Lin, Y. Zhu, X. Yu, J. Li, R. Lin, D. Nordlund, T.-C. Weng, R. M. Richards, X.-Q. Yang, *Nano Lett.* **2015**, *15*, 5755.
[263] P. Senguttuvan, G. Rousse, V. Seznec, J.-M. Tarascon, M. R. Palacin, *Chem. Mater.* **2011**, *23*, 4109.
[264] A. Rudola, K. Saravanan, S. Devaraj, H. Gong, P. Balaya, *Chem. Commun.* **2013**, *49*, 7451.
[265] A. Rudola, K. Saravanan, C. W. Mason, P. Balaya, *J. Mater. Chem. A* **2013**, *1*, 2653.
[266] W. Wang, C. Yu, Z. Lin, J. Hou, H. Zhu, S. Jiao, *Nanoscale* **2013**, *5*, 594.
[267] W. Zou, J. Li, Q. Deng, J. Xue, X. Dai, A. Zhou, J. Li, *Solid State Ionics* **2014**, *262*, 192.
[268] M. A. Muñoz-Márquez, M. Zarrabeitia, E. Castillo-Martínez, A. Eguía-Barrio, T. f. Rojo, M. Casas-Cabanas, *ACS Appl. Mater. Interfaces* **2015**, *7*, 7801.
[269] Y. Sun, L. Zhao, H. Pan, X. Lu, L. Gu, Y. S. Hu, H. Li, M. Armand, Y. Ikuhara, L. Chen, X. Huang, *Nat. Commun.* **2013**, *4*, 1870.
[270] J. Xu, C. Ma, M. Balasubramanian, Y. S. Meng, *Chem. Commun.* **2014**, *50*, 12564.
[271] C. Ling, R. Zhang, *Phys. Chem. Chem. Phys.* **2017**, *19*, 10036.
[272] G. Rousse, M. E. Arroyo-de Dompablo, P. Senguttuvan, A. Ponrouch, J.-M. Tarascon, M. R. Palacín, *Chem. Mater.* **2013**, *25*, 4946.
[273] H. Pan, X. Lu, X. Yu, Y.-S. Hu, H. Li, X.-Q. Yang, L. Chen, *Adv. Energy Mater.* **2013**, *3*, 1186.
[274] K. Shen, M. Wagemaker, *Inorg. Chem.* **2014**, *53*, 8250.
[275] J. Kim, J. Cho, *Electrochem. Solid-State Lett.* **2007**, *10*, A81.
[276] C. Ling, F. Mizuno, *Phys. Chem. Chem. Phys.* **2014**, *16*, 10419.
[277] M. Mortazavi, C. Wang, J. Deng, V. B. Shenoy, N. V. Medhekar, *J. Power Sources* **2014**, *268*, 279.
[278] E. Yang, H. Ji, J. Kim, H. Kim, Y. Jung, *Phys. Chem. Chem. Phys.* **2015**, *17*, 5000.
[279] Y.-X. Yu, *J. Phys. Chem. C* **2016**, *120*, 5288.
[280] Z. Xu, X. Lv, J. Li, J. Chen, Q. Liu, *RSC Adv.* **2016**, *6*, 25594.
[281] L. Shi, T. Zhao, A. Xu, J. Xu, *Sci. Bull.* **2016**, *61*, 1138.
[282] H. Wang, X. Lan, D. Jiang, Y. Zhang, H. Zhong, Z. Zhang, Y. Jiang, *J. Power Sources* **2015**, *283*, 187.
[283] X. Xie, Z. Ao, D. Su, J. Zhang, G. Wang, *Adv. Funct. Mater.* **2015**, *25*, 1393.
[284] A. Jain, S. P. Ong, G. Hautier, W. Chen, W. D. Richards, S. Dacek, S. Cholia, D. Gunter, D. Skinner, G. Ceder, *APL Mater.* **2013**, *1*, 011002.
[285] W. Li, Y. Ando, E. Minamitani, S. Watanabe, *J. Chem. Phys.* **2017**, *147*, 214106.
[286] C. Chen, Z. Deng, R. Tran, H. Tang, I.-H. Chu, S. P. Ong, *Phys. Rev. Mater.* **2017**, *1*, 043603.
[287] J. Behler, *J. Chem. Phys.* **2016**, *145*, 170901.